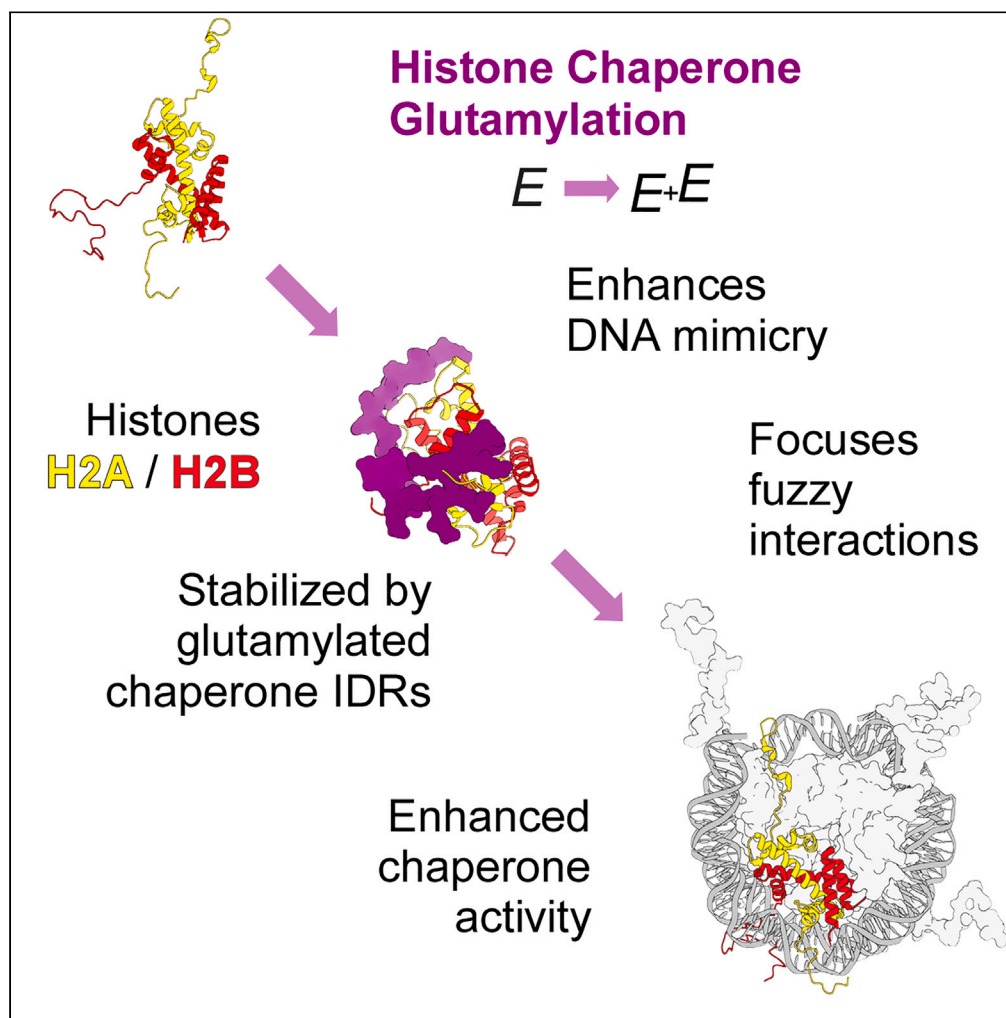


## Article

## Glutamylation of Npm2 and Nap1 acidic disordered regions increases DNA mimicry and histone chaperone efficiency



Benjamin M. Lorton,  
Christopher Warren, Humaira Ilyas, ..., Andras Fiser, David Cowburn, David Shechter

david.shechter@einsteinmed.edu

**Highlights**

Acidic IDRs in Npm2 and Nap1 act as DNA mimetics

TTL4 post-translationally glutamylates chaperone acidic IDRs

Glutamate-glutamylation of chaperone IDRs increases DNA electrostatic mimicry

NMR and MD studies reveal how glutamylated IDR binding enhances histone stability

Lorton et al., iScience 27, 109458  
April 19, 2024 © 2024 The Author(s).  
<https://doi.org/10.1016/j.isci.2024.109458>

## Article

## Glutamylation of Npm2 and Nap1 acidic disordered regions increases DNA mimicry and histone chaperone efficiency

Benjamin M. Lorton,<sup>1,7</sup> Christopher Warren,<sup>1,5,7</sup> Humaira Ilyas,<sup>1,7</sup> Prithviraj Nandigrami,<sup>1,4</sup> Subray Hegde,<sup>1</sup> Sean Cahill,<sup>1</sup> Stephanie M. Lehman,<sup>2,6</sup> Jeffrey Shabanowitz,<sup>2</sup> Donald F. Hunt,<sup>3</sup> Andras Fiser,<sup>1,4</sup> David Cowburn,<sup>1</sup> and David Shechter<sup>1,8,\*</sup>

## SUMMARY

**Histone chaperones—structurally diverse, non-catalytic proteins enriched with acidic intrinsically disordered regions (IDRs)—protect histones from spurious nucleic acid interactions and guide their deposition into and out of nucleosomes. Despite their conservation and ubiquity, the function of the chaperone acidic IDRs remains unclear. Here, we show that the *Xenopus laevis* Npm2 and Nap1 acidic IDRs are substrates for TTL4 (Tubulin Tyrosine Ligase Like 4)-catalyzed post-translational glutamate-glutamylation. We demonstrate that to bind, stabilize, and deposit histones into nucleosomes, chaperone acidic IDRs function as DNA mimetics. Our biochemical, computational, and biophysical studies reveal that glutamylation of these chaperone polyelectrolyte acidic stretches functions to enhance DNA electrostatic mimicry, promoting the binding and stabilization of H2A/H2B heterodimers and facilitating nucleosome assembly. This discovery provides insights into both the previously unclear function of the acidic IDRs and the regulatory role of post-translational modifications in chromatin dynamics.**

## INTRODUCTION

Nucleosomes—the complex of histone proteins and DNA that compacts and regulates the eukaryotic genome—are assembled in a tightly regulated process. Histone chaperones bind to the basic histone proteins (H2A, H2B, H3, H4, and H1 linker histones), promote proper nucleosome assembly, and reduce non-nucleosomal histone:nucleic acid interactions,<sup>1–3</sup> while ATP-dependent remodelers position the nucleosomes. To coordinate RNA polymerase passage, some chaperones like FACT engage both histones and assembled nucleosomes.<sup>4–6</sup> NMR analysis of human and *Drosophila* H2A/H2B heterodimers showed that, while the overall structure is similar to nucleosomal H2A/H2B, the histones in solution are dynamic.<sup>7,8</sup>

Despite performing common functions, the large family of histone chaperones are structurally diverse. As we previously showed, most contain long intrinsically disordered regions (IDRs) that are enriched with acidic stretches.<sup>9,10</sup> Structures of histone chaperones bound to their cognate histones have revealed common interaction themes, including an “anchoring and capping” mechanism of H2A/H2B-interacting histone chaperone acidic stretches.<sup>11–13</sup> Others have shown direct interactions and function of acidic IDRs with histones, including: the SPT16 subunit IDR of FACT interaction with H2A/H2B;<sup>5</sup> MCM2 acidic IDR interaction with Asf1 and H3/H4<sup>14,15</sup>; and on octamers by acidic IDRs of APLF.<sup>16</sup> Studies of the Nap1 chaperone:histone interactions are challenged both by its oligomeric nature and the likely multiple binding modes, but it has been demonstrated that histone interactions are enhanced by the presence of the Nap1 N- and C-terminal acidic IDRs.<sup>17–21</sup> A recent study further suggests that Nap1 acidic IDRs exhibit a “penetrating, fuzzy binding mechanism” to histones mediated by electrostatic interactions.<sup>22</sup>

$\gamma$ -Glutamate-glutamylation is a reversible post-translational modification (PTM) catalyzed by an ATP-dependent addition of a glutamate amino acid to an existing peptidyl glutamate.<sup>23</sup> The initiator glutamate is added to the  $\gamma$ -carboxyl group of a glutamate sidechain through an isopeptide bond. Additional glutamates can be added either to the  $\alpha$ -carboxyl or  $\gamma$ -carboxyl groups of the branchpoint glutamate, resulting in polyglutamylation. The family of Tubulin Tyrosine Like Ligase (TTL) enzymes catalyze glutamylation,<sup>23</sup> while deglutamylation is catalyzed

<sup>1</sup>Department of Biochemistry, Albert Einstein College of Medicine, Bronx, NY 10461, USA

<sup>2</sup>Department of Chemistry, University of Virginia, Charlottesville, VA 22908, USA

<sup>3</sup>Departments of Chemistry and Pathology, University of Virginia, Charlottesville, VA 22908, USA

<sup>4</sup>Department of Systems & Computational Biology, Albert Einstein College of Medicine, Bronx, NY 10461, USA

<sup>5</sup>Present address: Merck & Co., Inc., 2025 E Scott Ave., Rahway, NJ 07065

<sup>6</sup>Present address: GSK, Collegeville, Pennsylvania 19426

<sup>7</sup>These authors contributed equally

<sup>8</sup>Lead contact

\*Correspondence: david.shechter@einsteinmed.edu

<https://doi.org/10.1016/j.isci.2024.109458>



by members of the Cytosolic Carboxypeptidase (CCP) enzyme family.<sup>24</sup> Glutamylation was first identified on alpha and beta tubulin,<sup>25–27</sup> where it modulates interactions with microtubule associated proteins, thereby influencing the dynamics of microtubule arrays in cells.<sup>28</sup> Glutamylation was also identified on histone chaperones, including Nucleophosmin (NPM1),<sup>29</sup> Nucleoplasmin (Npm2),<sup>30</sup> Nucleosome Assembly Proteins 1 and 2 (Nap1, Nap2), Acidic Nuclear Phosphoprotein 32 E (ANP32E),<sup>31–33</sup> and PELP1.<sup>34</sup> While one study demonstrated that glutamylation of the C-terminal acidic domain of Nap1 increased deposition of linker histones and was required for condensation of mitotic chromosomes,<sup>31</sup> how glutamylation influences chaperone function remains largely unknown.

The fundamental mechanisms underlying the transfer of histones from chaperone to DNA remain largely unknown.<sup>35–38</sup> Recent studies have implicated long-timescale dynamic polyelectrolyte competition in chaperone IDR mediation of H1 linker histone removal.<sup>39</sup> In light of this and related observations on the cellular function of diffuse and multivalent charge-charge interactions,<sup>40,41</sup> we suggest that intermediate, electrostatically mediated states are likely critical for the ordered formation and disassembly of nucleosomes. To understand histone chaperone mechanisms, we hypothesized that chaperone acidic IDRs—made more acidic by glutamate-glutamylation—mimic DNA to promote histone stability and enhance histone deposition and removal. In this study, we provide robust computational, biochemical, and biophysical evidence that post-translationally glutamylated histone chaperone acidic IDRs behave as polyelectrolytes to bind to histones. This binding stabilizes H2A/H2B for either nucleosomal deposition or for aggregate removal.

## RESULTS

### Nap1 and Npm2 are glutamate-glutamylated

Due to their abundance in *Xenopus laevis* eggs and their well described and widely conserved function in histone storage and deposition, we focused on the canonical H2A/H2B chaperones Npm2 (also known as Nucleoplasmin) and Nap1 (NAP1L1, Nucleosome Assembly Protein 1 Like 1, here referred to as Nap1). We previously showed that Npm2 from *Xenopus laevis* eggs and oocytes was glutamylated within the A2 acidic disordered stretch<sup>30</sup> (Figures 1A and 1B). Here, we purified Nap1 from *Xenopus* egg extract and showed that it is post-translationally glutamylated (Figures 1A, 1B, and S1A–S1E). As observed by immunoblot and mass spectrometry (Figure S1F), *Xenopus* Nap1 has two main genetic isoforms (Nap1.S and Nap1.L) and two splice isoforms (X1 and X2). The X1 isoform contains ten additional residues at its C-terminus and harbors a single farnesyl-cysteine that is not present on isoform X2 (Figure 1C, highlighted green). In this study, we used the most abundant isoform (X2; Figure S1G). We identified Nap1 mono-glutamylation within both its N-terminal A1 and C-terminal A3 acidic disordered stretches (Figure 1C, highlighted orange). Glutamylation of the Nap1 A1 acidic stretch occurs in distribution (one to six sites, with three most abundant at 30–50% of total protein) (Figures 1D and 1F). The Nap1 A3 acidic patch contained one to eleven sites of glutamylation, with eight sites being the most abundant form at 30–50% of total protein (Figures 1E and 1F). While outside of our Npm2 and Nap1 experiments in this study, we also observed by immunoblot that the egg histone chaperone NASP (formerly known as N1) was glutamylated (Figures S1H and S1I).

To define the physical nature of monoglutamylation, we computationally modeled both glutamate and  $\gamma$ -glutamyl-glutamate. The unmodified glutamate sidechain measures 4.86 Å in length with a surface area of 91 Å<sup>2</sup>, and a predicted pK<sub>a</sub> of 4.51 ± 0.22 for the  $\gamma$ -carboxyl group (Figure 1G and Data S1). The  $\gamma$ -glutamyl-glutamate side chain was more than doubled in length and surface area, measuring 10.35 Å and 202.67 Å<sup>2</sup>, respectively, and contained an additional negative charge; the carboxyl groups predicted pK<sub>a</sub>'s are 4.79 ± 0.22 and 3.65 ± 0.63 (Figure 1H). Thus, glutamylation dramatically increased the size and acidic character of the glutamate side chain (Data 1 for models).

### Histone chaperone intrinsically disordered acidic tails are important for histone binding

To test the contributions of the Nap1 intrinsically disordered acidic tails to histone binding, we performed a competitive pull-down assay using H2A.S2/H2B heterodimers (H2A contained a C-terminal StrepII-tag, denoted S2) and Nap1 full-length or truncations lacking either or both A1 or A3 acidic tails (Figure 2A). In the pull-downs, all four proteins bound H2A.S2/H2B. In the competition assays, both full-length and Nap1  $\Delta$ A1 interacted with H2A.S2/H2B better than did the Nap1  $\Delta$ A3 or Nap1-core domain proteins; Nap1  $\Delta$ A3 and Core domain bound histones with relative equal affinity. These results show that the C-terminal A3 acidic stretch increases relative Nap1 affinity for histones.

To assess the role of the acidic tails on the ability of Nap1 to resolve histone-DNA aggregates, we utilized a histone-capturing disaggregation assay (Figure 2B). Using a 500bp linear fragment of double-stranded DNA (dsDNA) mixed with a 20-fold molar excess of H2A/H2B heterodimer, we produced a non-nucleosomal histone-DNA aggregate solution. Upon addition to the aggregates, full-length Nap1 captured nearly all histones, resulting in complete recovery of free DNA. The Nap1  $\Delta$ A1 construct was partially able to recover free DNA, whereas Nap1  $\Delta$ A3 and Core domains were not sufficient to capture histones. These results indicate that both A1 and A3 acidic stretches of Nap1 increase histone binding affinity and are important for its ability to resolve histone-DNA aggregates.

To evaluate the role of the acidic stretches on the ability of Nap1 and Npm2 to form nucleosomes, we utilized a mononucleosome assembly assay (Figures 2C and 2D). Tetrasomes—recombinant H3/H4 assembled with 187 bp of dsDNA by salt dilution—were subsequently mixed with Nap1 or Npm2 prebound to increasing concentrations of H2A/H2B heterodimers; salt-dialysis assembled nucleosomes were included as a positive control. Using increasing concentrations of Nap1 bound to constant H2A/H2B-Alexa488 dimers mixed with tetramer substrates, we confirmed specific chaperone-dependent H2A/H2B incorporation into nucleosomes (Figures S2A and S2B). Subsequent experiments therefore used the nucleosome DNA position as a standard. Full-length Nap1 and the  $\Delta$ A1 construct both formed nucleosomes to a similar extent, whereas  $\Delta$ A3 did so to a lesser degree; the core domain was incapable of assembling nucleosomes (Figures 2C and S2C). As we previously showed,<sup>9</sup> full-length Npm2 contains a C-terminal basic patch that self-associates to block its acidic histone-binding domain. Histone binding is recovered when this basic patch is truncated (Npm2 core+A2). Much like the Nap1 core domain, we previously showed that the Npm2 core

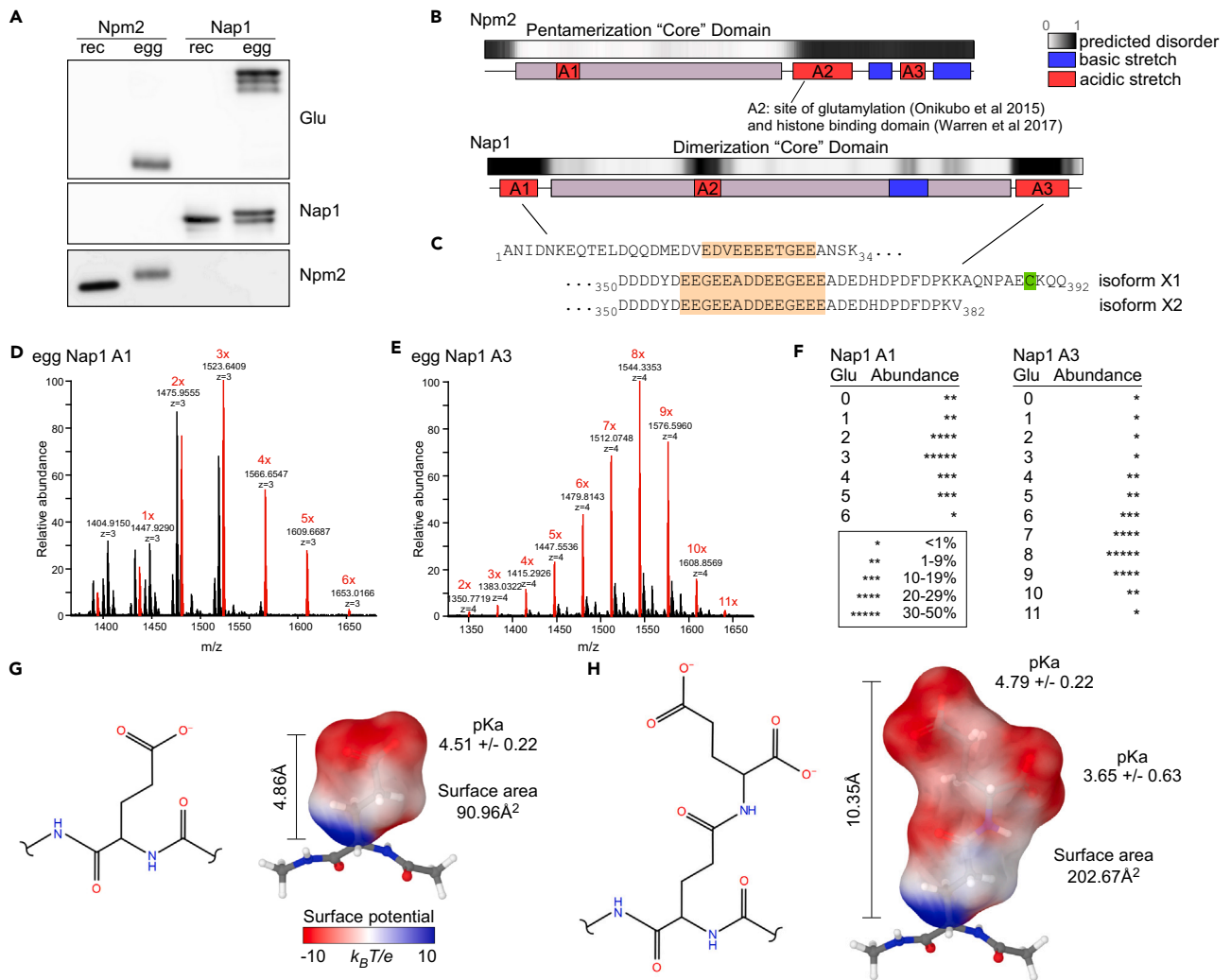


**Figure 1. *Xenopus laevis* histone chaperones Npm2 and Nap1 are glutamate-glutamylated on their acidic IDRs**

(A) Recombinant (rec) and purified egg Npm2 and Nap1 were immunoblotted for glutamylation (glu, top), Nap1 (middle), and Npm2 (bottom) showing glutamylation specifically on endogenous chaperones.

(B) Predicted disorder (black and white) and domain maps of Npm2 (top) and Nap1 (bottom) showing acidic (red) and basic (blue) patches coincident with intrinsically disordered tails.

(C) Sites of glutamylation (highlighted orange) detected by mass spectrometry on endogenous Nap1 purified from *Xenopus* eggs. A single farnesyl cysteine (highlighted green) was detected in the longer Nap1 X1 isoform.

(D) Quantification of glutamylation on Nap1 acidic patch A1 detected by mass spectrometry.

(E) Quantification of glutamylation on Nap1 acidic patch A3 detected by mass spectrometry.

(F) Relative abundance of Nap1 A1 and A3 glutamylation determined from mass spectrometry.

(G) Model of a peptidyl glutamate showing stick and electrostatic surface potential representations.

(H) Same as (G) but model of post-translational glutamate-glutamylated.

domain retains its ability to bind histones. Consistently, only the Npm2 Core+A2 bound to H2A/H2B formed nucleosomes on a tetrasome substrate (Figures 2D and S2D). Together, these experiments demonstrate that, while the Nap1 and Npm2 acidic tails are dispensable for histone binding, they are required for their histone chaperoning functions of disaggregation and nucleosome assembly.

### Chaperone glutamylation enhances histone binding and promotes histone stabilization

We next sought to investigate the molecular function of post-translational glutamylation of histone chaperones. First, both Npm2 core+A2 and full-length Nap1 proteins were post-translationally glutamylated by recombinant human Tyrosine Tubulin Like Ligase 4 (TTL4) catalytic domain (Figure S3A). All TTL4-treated proteins are hereafter referred to with the suffix "glu". As we previously showed, recombinant

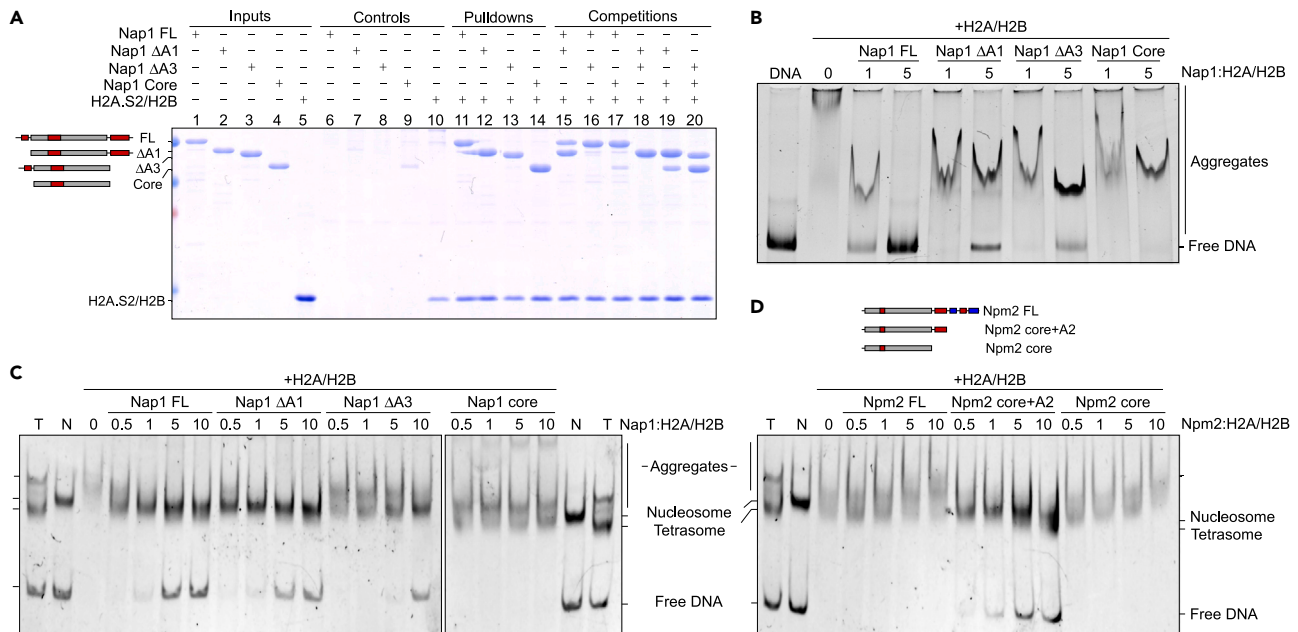


**Figure 2. Histone chaperone acidic IDRs maximize histone binding, facilitate disaggregation, and promote nucleosome assembly**

(A) StrepII-tagged H2A.S2/H2B pull-down and competition binding assays of Nap1 truncation mutants. Coomassie stained gel with components included as indicated at the top. Left-graphic shows domain structure of the Nap1 truncations, with gray indicating the core domain and red indicating acidic IDRs. (B) Histone-capturing disaggregation assay from histone-DNA aggregates using Nap1 truncation mutants. Molar ratio of monomeric chaperone to H2A/H2B is shown. (C) Mononucleosome assembly assay starting from tetrasome (T) using H2A/H2B dimers and Nap1 truncation mutants. Nucleosome (N) included as positive control. The location on the gel of the Nucleosome, Tetrasome, and Free DNA are indicated. molar ratio of monomeric chaperone to H2A/H2B is shown. (D) Same as (C) but using Npm2 truncation mutants.

full-length Npm2 is not a substrate for TTL4.<sup>30</sup> Therefore, in these experiments we used the Npm2 core+A2 protein. As we previously showed for Npm2 core+A2,<sup>9</sup> the presence of histones H2A/H2B blocked TTL4 glutamylation of Nap1, consistent with acidic IDR substrates engaging histone binding (Figure S3B). Glutamylation did not alter the oligomeric state of full-length Nap1 (Figure S3C).

To test relative interactions, we utilized the H2A.S2/H2B competition pull-down assay with unmodified or glutamylated Npm2 core+A2 and Nap1 proteins (Figure 3A). Protein glutamylation resulted in a slight gel retardation (Figure 3A, lanes 2 and 4). As a positive control, all four proteins were pulled down by H2A.S2/H2B (Figure 3A, lanes 11–14). Unmodified Nap1 had a higher relative affinity compared to Npm2 core+A2 (Figure 3A, lane 15). When competed against unmodified proteins, both Npm2 Core+A2glu and Nap1glu have a higher relative affinity for H2A.S2/H2B (Figure 3A, lanes 16 and 17). Both glutamylated proteins have similar affinities for H2A.S2/H2B (Figure 3A, lane 18). Note that, as Npm2 is a pentamer while Nap1 is likely an oligomer-of-dimers, avidity effects complicate direct affinity comparisons. Overall, these results demonstrate that glutamylation of Npm2 core+A2 and Nap1 increases their relative affinities for H2A.S2/H2B.

We previously demonstrated that, compared to the complete Npm2 Tail, the short Npm2 A2 peptide (<sup>122</sup>DYSWAE<sup>E</sup>E<sup>E</sup>DE<sup>131</sup>) had relatively weak affinity toward H2A/H2B.<sup>9</sup> Therefore, we reasoned that glutamylation of this region would substantially increase affinity of Npm2 toward H2A/H2B dimers. To test this, we performed quantitative intrinsic tryptophan fluorescence H2A/H2B binding assays. This assay measures binding-induced environmental changes to the A2 peptide tryptophan. We used the following synthetic unmodified and glutamylated Npm2 A2 peptides: A2glu1-DYSWAE<sup>E</sup>DE; A2glu2-DYSWAE<sup>E</sup>E<sup>E</sup>DE; A2glu4-DYSWAE<sup>E</sup>E<sup>E</sup>E<sup>E</sup>DE; and A2mockglu4 DYSWAE<sup>E</sup>E<sup>E</sup>E<sup>E</sup>E<sup>E</sup>DEE, where the superscripted E<sup>E</sup> denotes sites of glutamate-glutamylation (Figure 3B). These experiments showed that, while the unmodified A2 peptide binds to H2A/H2B with modest affinity ( $K_D = 22.6 \pm 4.4\mu\text{M}$ ), there was a glutamylation-dependent increase in histone affinity: A2glu1 ( $K_D = 9.1 \pm 2.4\mu\text{M}$ ), A2glu2 ( $K_D = 5.8 \pm 1.4\mu\text{M}$ ), A2glu4 ( $K_D = 0.4 \pm 0.1\mu\text{M}$ ); maximal glutamylation increased the affinity of this peptide toward H2A/H2B by approximately two orders of magnitude.

To separate the effects of specific contacts made due to the branched nature of glutamylation from non-specific electrostatic effects from the extra negative charge on the region, we tested the binding of an A2mockglu4 peptide with 4 extra glutamates added in the primary sequence through normal peptide bonds (DYSWAE<sup>E</sup>E<sup>E</sup>E<sup>E</sup>E<sup>E</sup>DEE). We observed that this “pseudo-glutamylated” Npm2 peptide bound to H2A/H2B dimers with high affinity, like that of the glutamylated version ( $K_D = 0.3 \pm 0.1\mu\text{M}$ ). This result indicated that electrostatic effects may explain the increased affinity observed with the glutamylated peptides.

As histones in solution may be less ordered than when bound to DNA in the nucleosome, we hypothesized that glutamylated acidic IDRs may serve to stabilize the histone fold. To determine if chaperone binding and their post-translational glutamylation increases the thermal stability of H2A/H2B dimers, we performed protein thermal shift melting assays in the absence and presence of various Npm2 and Nap1



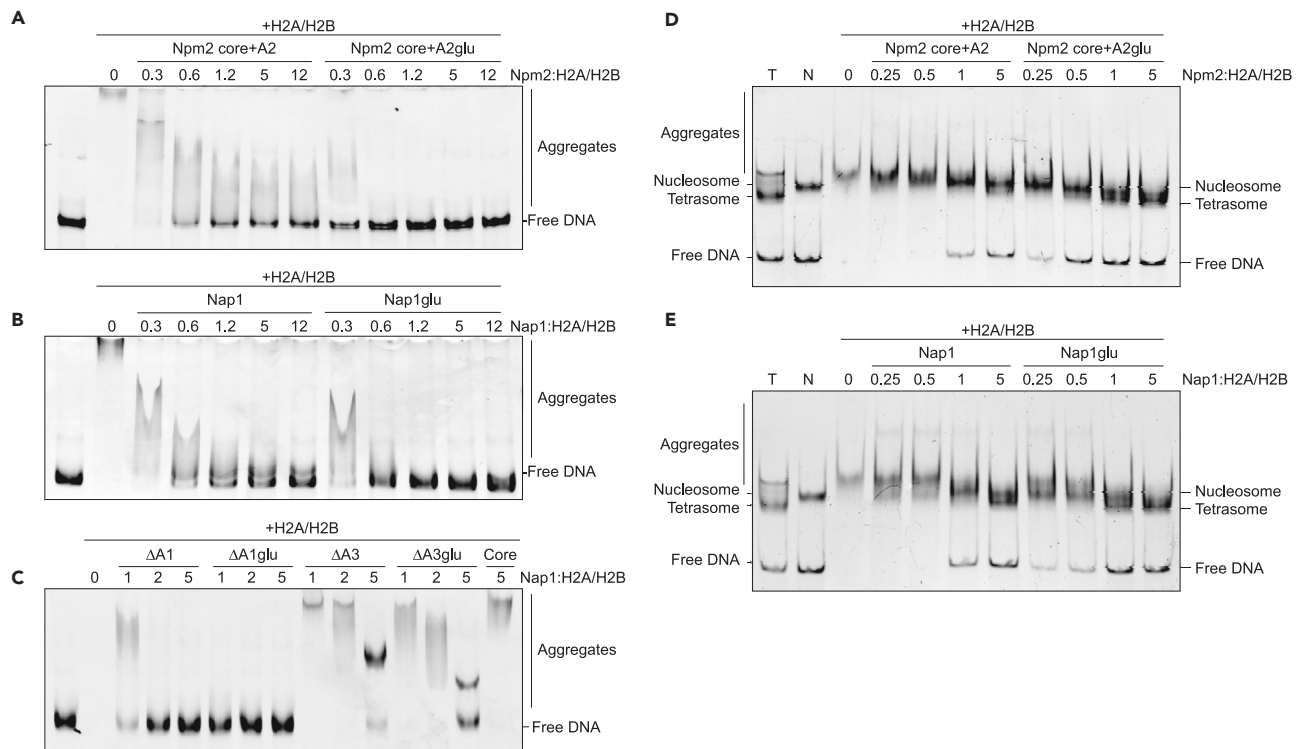


**Figure 4. Npm2 and Nap1 glutamylation enhances histone capture and promotes mononucleosome assembly**

(A) Histone-capturing disaggregation assay from histone:DNA aggregates using either unmodified or glutamylated Npm2 core+A2. Chaperones were titrated as indicated, molar ratio of monomeric chaperone to H2A/H2B is shown.

(B) Histone-capturing disaggregation assay from histone:DNA aggregates using either unmodified or glutamylated Nap1, molar ratio of monomeric chaperone to H2A/H2B is shown.

(C) Histone-capturing disaggregation assay from histone:DNA aggregates using either unmodified or glutamylated Nap1 truncation mutants, molar ratio of monomeric chaperone to H2A/H2B is shown.

(D) Mononucleosome assembly assay starting from pre-assembled tetrasomes using H2A/H2B dimers and unmodified Npm2 core+A2 and TLL4-treated Npm2 core+A2 (Npm2 Core+A2 glu), molar ratio of monomeric chaperone to H2A/H2B is shown.

(E) Mononucleosome assembly assay starting from pre-assembled tetrasomes using H2A/H2B dimers and unmodified Nap1 and TLL4-treated Nap1 (Nap1glu), molar ratio of monomeric chaperone to H2A/H2B is shown.

### Glutamylation promotes histone chaperone activity

As we demonstrated that chaperone acidic IDRs and their glutamylation enhances histone binding and stabilization, we hypothesized that it is a potential regulatory PTM for promoting chaperone efficiency. Therefore, our next goal was to investigate how glutamate-glutamylation alters histone chaperone function. To this end, we used both the histone-capturing disaggregation and mononucleosome assembly (Figure S4A) functional assays. While both unmodified Npm2 core+A2 and Nap1 were able to partially resolve the histone-DNA aggregates, their glutamylated counterparts completely captured histones from the aggregate at a lower chaperone:H2A/H2B ratio (Figures 4A and 4B, respectively). Although the Nap1 A1 and A3 acidic patches were dispensable for low-affinity histone binding (Figure 2A), we tested the effect glutamylation has on the Nap1 truncations with respect to capturing histones from the DNA aggregate (Figure 4C). Glutamylation of Nap1  $\Delta A1$  dramatically increased histone capture in the 1:1 Nap1:H2A/H2B ratio experiment, unmodified  $\Delta A1$  modestly recovered free DNA, and glutamylated  $\Delta A1$  completely resolved aggregation. The Nap1  $\Delta A3$  truncation showed a similar effect: in the 5:1 Nap1:H2A/H2B ratio experiment, glutamylated Nap1  $\Delta A3$  recovered more free-DNA than did its unmodified counterpart. Even though both Npm2 and Nap1 can bind to H3/H4, neither chaperone with or without glutamylation could disaggregate H3/H4 bound to the same DNA (Figures S4B and S4C). While short DNA fragments were unable to remove Nap1 or Nap1glu from H2A.S2/H2B (Figure S4D), these results are generally consistent with acidic tails competing with DNA for histones and with the hypothesis that glutamylation enhances this competition by increasing DNA mimicry.

Finally, to measure glutamylation-induced changes in nucleosome assembly activity, we used the tetrasome-deposition assay as described above. In line with the disaggregation assay, glutamylation of Npm2 core+A2 enhanced H2A/H2B deposition on tetrasomes to assemble nucleosomes (Figure 4D, compare 0.25 and 0.5 M ratios in control and TLL4 treated samples). Similarly, glutamylation of Nap1 enhanced deposition of H2A/H2B on tetrasomes (Figure 4E, compare 0.25 and 0.5 M ratios in control and TLL4 treated samples); however,

neither Nap1 nor Nap1glu were able to disassemble premade mononucleosomes (Figure S4E). Taken together, these results strongly demonstrate that the intrinsically disordered acidic tails of Npm2 and Nap1 are critical for histone chaperoning activity and that glutamylation amplifies their efficiency.

### Molecular dynamics simulations reveal modes of acidic IDR binding to the H2A/H2B heterodimer

To understand how acidic IDRs and glutamylation mechanistically influence chaperone:histone binding and also affect histone protein stabilization, we first used computational approaches. To predict structural changes and contacts that occur upon binding, we performed one microsecond, all-atom, explicit solvent molecular dynamics simulations of the H2A/H2B heterodimer in complex with unmodified or fully-glutamylated Npm2 A2 or A2glu4 (<sup>122</sup>DYSWAEEED<sup>131</sup>) or in complex with Nap1 A3 or A3glu9 (<sup>350</sup>DYDEEGEEADDEEGEEADEDHDPDFDK<sup>382</sup>) peptides; underscored residues correspond to sites of modeled glutamylation. Each trajectory was performed twice, from distinct starting positions; representations are shown from a single simulation (Videos S1, S2, S3, S4, and S5).

As demonstrated in solution with our thermal shift assay (Figures 3C–3F), binding of the Npm2 A2glu4, Npm2 119–146aa, and Nap1 350–382aa peptides all resulted in significant stabilization of the H2A/H2B heterodimer. To assess how glutamylation of Npm2 A2 and Nap1 350–382aa affected histone stabilization, across the trajectories we measured the average fluctuation of each residue of the H2A/H2B dimer, either in its apo form or bound to either unmodified or glutamylated Npm2 A2 or Nap1 peptides (Figures 5A and 5B, respectively). In the simulation, both unmodified peptides stabilized the H2A/H2B dimer—compare apo (blue lines) to unmodified peptides (gray lines)—showing reduced fluctuations across both histone folds. Notable stabilization ranging from the terminal end of the H2A  $\alpha$ 1 through the  $\alpha$ 3 helices was observed upon interaction with Npm2 A2 or Nap1 A3 peptides; additional stabilization at the H2A  $\alpha$ C helix occurs with Npm2 A2 interaction. Both unmodified Npm2 A2 and Nap1 peptides also reduced fluctuations across the entire H2B fold, ranging from  $\alpha$ 1 through  $\alpha$ C helices. Compared to its unmodified counterpart, the glutamylated Npm2 A2glu4 peptide (Figure 5A, orange lines) further reduced fluctuations of H2A, ranging from  $\alpha$ 2 through  $\alpha$ 3 helices and had a modest effect on H2B stability. Compared to unmodified Nap1, in the simulation the Nap1 A3glu9 peptide (Figure 5B, orange lines) also increased stability of the H2A  $\alpha$ 3 to  $\alpha$ C helices; it also stabilized the  $3_{10}$  helix at the H2A C-terminus. Likewise, in the trajectory Nap1glu9 reduced fluctuations in the H2B  $\alpha$ 2 helix and had modest effect between  $\alpha$ 3 and  $\alpha$ C helices. Overall, *in silico*, glutamylation of Npm2 and Nap1 reduced fluctuations and stabilized both H2A and H2B histone folds.

To understand why the glutamylated peptides stabilize the histones, we measured how they interacted. Over the course of the trajectory, the frequency of atomic contacts with the H2A/H2B dimer was both markedly localized and increased by glutamylation of both peptides. We measured the frequency of contact (defined  $<3.5$  Å) between each histone amino acid and any chaperone peptide amino acid. As shown in Figures 5C and 5D, glutamylated chaperone peptides (orange) made more frequent contact with localized histone residues than did non-glutamylated peptides (gray); these contact regions were remarkably similar to histone:DNA contacts ( $<3.5$  Å) in the nucleosome core particle (Figures 5C and 5D, bottom domain cartoon, orange lines). Across the trajectories, the unmodified Npm2 A2 peptide resulted in a distribution with a mean of 61 contacts (Figure 5E, gray bars), whereas the Npm2 A2glu4 peptide shifted this mean to approximately 125 contacts (orange bars). Likewise, the unmodified Nap1 A3 peptide showed a contact distribution with a mean of 166 contacts (Figure 5F, gray bars), and the Nap1 A3glu9 peptide shifted the mean to 268 atomic contacts (orange bars).

The effect of glutamylation is also highlighted by differences in the number and population of dominant conformational clusters of the IDR peptides. A density-based conformational clustering analysis showed that the Npm2 A2 peptide forms seven major clusters, with the top populated cluster accounting for 40% of the total population and the next five being similarly populated (Figure 5G, gray bars). The A2glu4 had better defined conformations, with only 4 major clusters; the most populated cluster contains almost all the conformations at approximately 70% of the total population (Figure 5G, orange bars). Similarly, simulation of the Nap1 A3 peptide binding H2A/H2B resulted in over a dozen sparsely populated clusters, with the top populated cluster accounting for only 20% of the total population (Figure 5H, gray bars). The Nap1glu9 peptide had just five clusters, with the top accounting for nearly 75% of the total population (Figure 5H, orange bars). These data strongly suggest that glutamylation of these peptides increases both the overall affinity and specificity of histone interactions.

Simulations with the Nap2 A2glu4 or Nap1glu9 peptides showed that Npm2 A2glu4 contacts H2A K15, T16, R17, G28, R29, R32, and K36 and H2B R33. Nap1glu9 contacts H2A K13, A14, K15, T16, R17, G28, R29, and R32 and H2B R30, T32, R33, K34, and I39 (Figure 5I). The two glutamylated peptides showed significant overlap with respect to the residues they contact (Figure 5G). Despite positioning the peptides randomly and distal from this location at the start of each simulation (Videos S1, S2, S3, S4, and S5), in both simulations both peptides found the same H2A binding pocket early in the MD trajectory (Figures 5J–5L). Supporting the idea that histone chaperone acidic stretches are in direct competition with DNA for histone interaction, this pocket coincides with the residues that directly contact the phosphate backbone of DNA and are positively charged in the nucleosome crystal structure (Figures 5I and 5M). Together, the results of our MD simulations predict a model in which glutamylation of histone chaperone acidic stretches results in stabilization of H2A/H2B through increased, specific histone residue contacts (Figures S5A–S5G).

### Solution NMR assignment and secondary structure of the *Xenopus* H2A/H2B heterodimer

NMR-studies of the human and *Drosophila* H2A/H2B dimers revealed that, while dynamic in solution, H2A/H2B adopts a similar overall fold as in the nucleosomal counterpart.<sup>7,8</sup> To test the solution structure and characteristics of *Xenopus* H2A/H2B, we individually labeled either H2A or H2B and formed the dimer with its unlabeled counterpart; these isotopically triple labeled dimers were [U-<sup>13</sup>C, <sup>15</sup>N, <sup>2</sup>H]-H2A/H2B and H2A/[U-<sup>13</sup>C, <sup>15</sup>N, <sup>2</sup>H]-H2B. Using TROSY-style triple-resonance experiments, we assigned 82% of possible C $\alpha$ , C $\beta$ , CO, HN, and N chemical shift values for H2A, and 74% of possible C $\alpha$ , C $\beta$ , CO, HN, and N chemical shift values for H2B. The unstructured tails of both H2A/H2B were

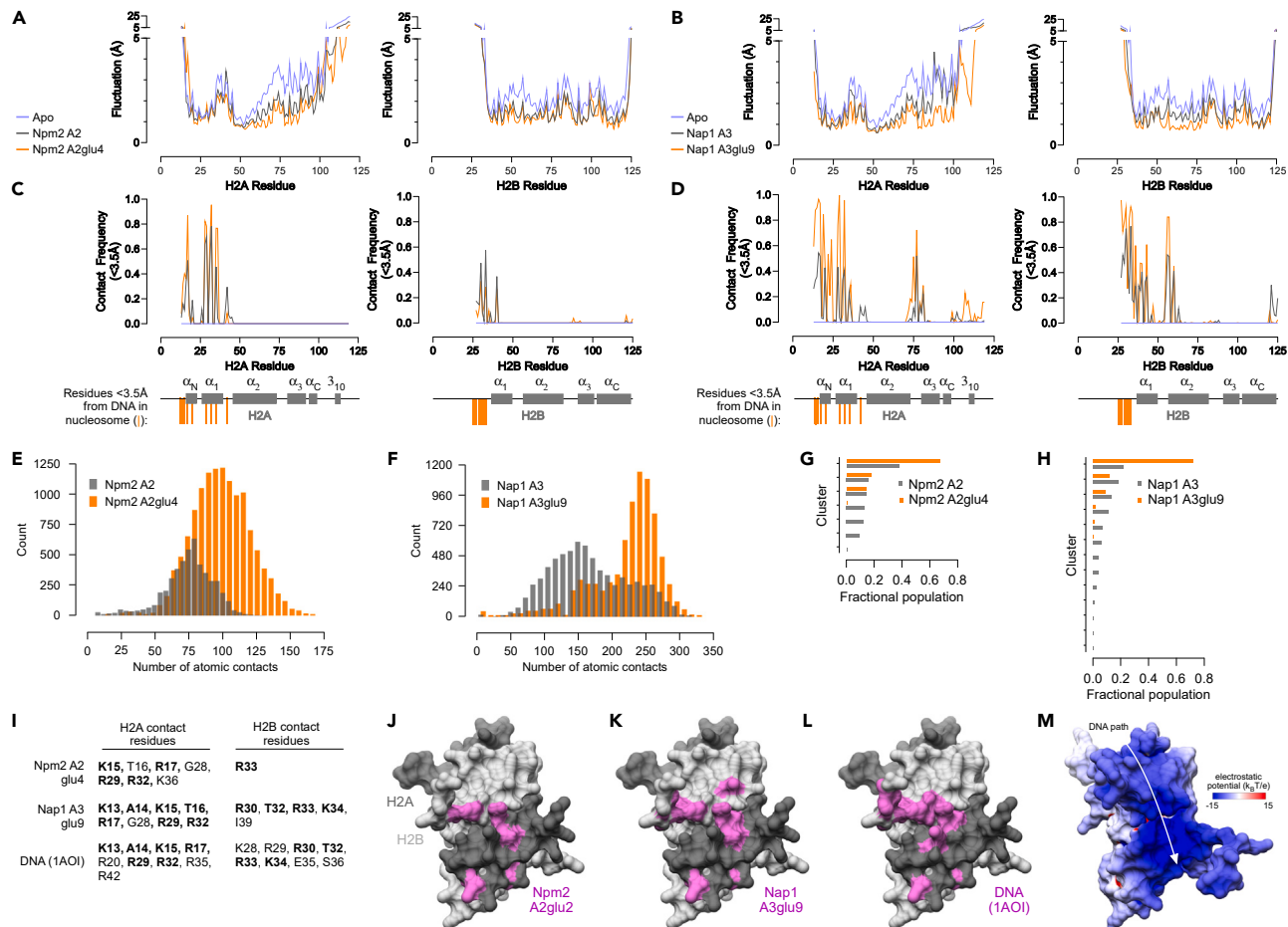


**Figure 5. All-atom, 1  $\mu$ s explicit solvent, molecular dynamics simulations show that Npm2 A2 and Nap1 A3 glutamylation stabilizes histones upon interaction**

(A) Average fluctuation plots of histone residues (H2A (left) and H2B (right)) in the apo (blue), Npm2 A2 (gray) or Npm2 A2glu4 (orange) complexes. (B) Same as in (A) but for Nap1 A3 (gray) and Nap1 A3glu9 (orange). (C) Interacting residues between Npm2 A2glu4 or Nap1 A3glu9 and H2A (top) and H2B (bottom); bolded residues are common histone residue contacts between both peptides. Bottom H2A and H2B domain maps, orange vertical lines indicate residues  $<3.5$  Å from DNA in the nucleosome (PDB:1A0I). (D) Same as in (C) but for Nap1 A3 (gray) or Nap1 A3glu9 (orange). (E) Distribution of atomic contacts between H2A/H2B and Npm2 A2 (gray) or Npm2 A2glu4 (orange). (F) Same as in (E) but for Nap1 A3 (gray) or Nap1 A3glu9 (orange). (G) Density-based conformational clustering of Npm2 A2 (gray) or Npm2 A2glu4 (orange) conformations when interacting with H2A/H2B. (H) Same as in (G) but for Nap1 A3 (gray) or Nap1 A3glu9 (orange). (I) Table of H2A (left) and H2B (right) residues with average distance over the MD trajectories  $<3.5$  Å distance to histone chaperone peptides. (J) Representative models from the most dominant clusters for Npm2 A2glu4 complexes with H2A/H2B. Pink indicates contact residues highlighted in (I). (K) Same as (J) but for Nap1 A3glu9. (L) Model of H2A/H2B and DNA from the nucleosome crystal structure (PDB: 1A0I). Pink indicates residues  $<3.5$  Å from DNA. (M) Electrostatic potential representation of the H2A/H2B dimer. The path of the DNA in the nucleosome core particle is indicated (arrow).

challenging to assign; overall, we assigned 93% of H2A and 85% of H2B residues from the folded histone core in the HSQC-spectra (Figures 6A and 6B, respectively).

To ascertain the stability of the individually labeled dimers, we also performed variable-temperature (VT) NMR experiments. We recorded a series of  $^1\text{H}$ - $^{15}\text{N}$  HSQC spectra of the unbound  $[\text{U-}^2\text{H}, ^{15}\text{N}]$ -H2A/H2B and H2A/ $[\text{U-}^2\text{H}, ^{15}\text{N}]$ -H2B dimers as a function of temperature (40°C, 25°C, 16°C, 10°C and 4°C). Temperature-induced changes in protein dynamics and from conformational exchange processes result in line broadening and chemical shifts in NMR spectra. Lowering the temperature of these samples showed near linear decreases in peak intensities for nearly all residues within the histone fold, while peaks corresponding to residues of the histone tails remained intense at lower temperatures (Figures S6A and S6B). In contrast, when raised to 40°C, peak broadening and CSP occurred globally. This could be attributed to the temperature induced increase in the thermal motion of atoms, which causes more mobility and thus line broadening effect, while CSPs appear

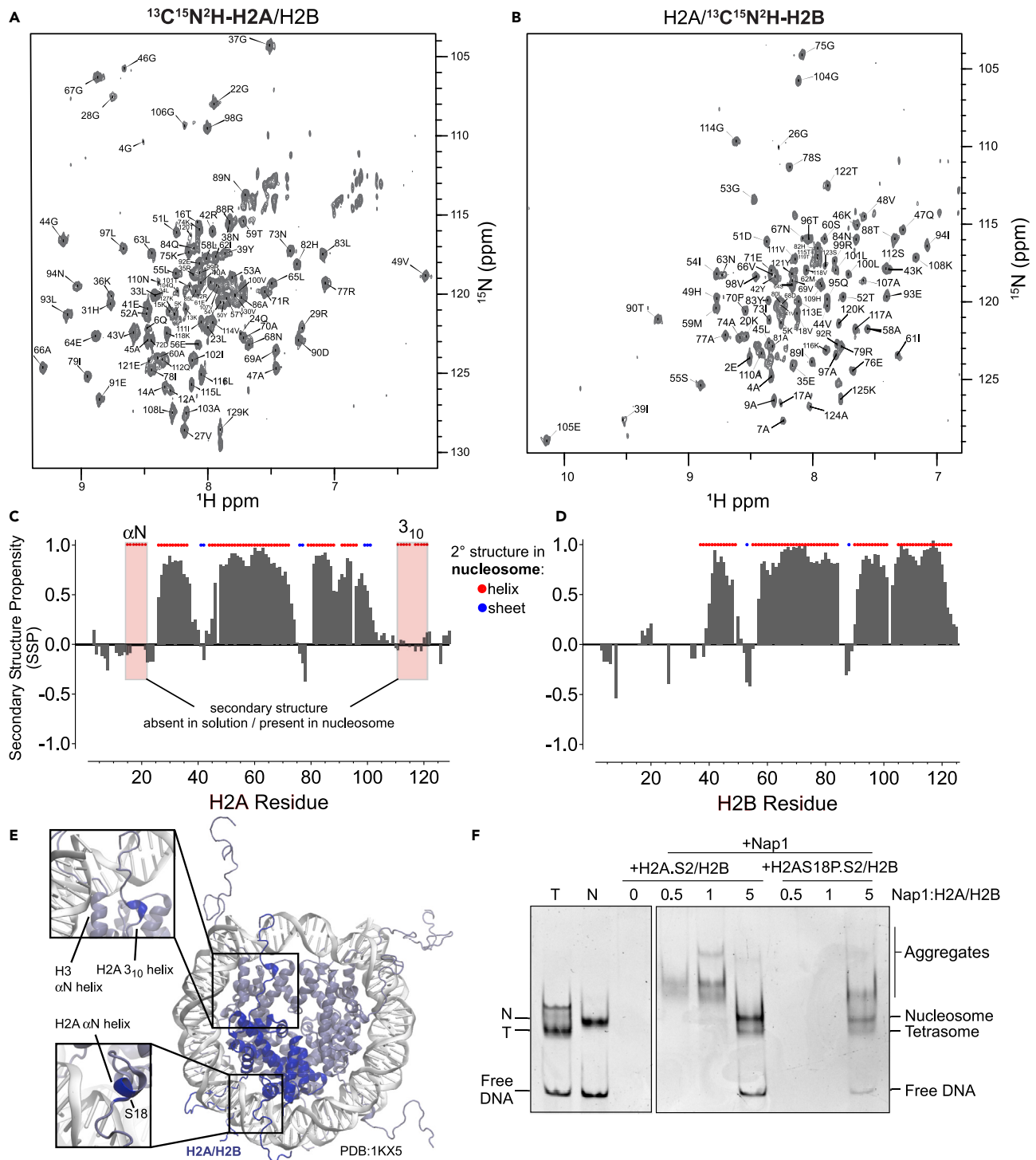


**Figure 6. Solution NMR analysis of the *Xenopus laevis* H2A/H2B dimer reveals secondary structure differences with the nucleosome**

(A) Assigned  $^1\text{H}$ - $^{15}\text{N}$ -TROSY-NMR spectra of triple labeled  $^2\text{H}$ - $^{13}\text{C}$ - $^{15}\text{N}$ -H2A in complex with H2B.

(B) Assigned  $^1\text{H}$ - $^{15}\text{N}$ -TROSY-NMR spectra of triple labeled  $^2\text{H}$ - $^{13}\text{C}$ - $^{15}\text{N}$ -H2B in complex with H2A.

(C) Secondary structure propensity (SSP) of H2A (histogram) compared with secondary structure of H2A in nucleosome (red dots = helical residues; blue dots = beta sheet).

(D) Same as (C) but for H2B.

**Figure 6. Continued**

(E) Representation of nucleosome core particle (PDB:1KX5) with H2A/H2B chains C,D shown in blue (center). Bottom inset shows the H2A  $\alpha$ N helix adjacent to DNA. Top inset shows H2A C-terminal  $3_{10}$  helix adjacent to the H3  $\alpha$ N helix.

(F) Mononucleosome assembly assay starting from pre-assembled tetrasomes using wildtype H2A.S2/H2B (left) or S18P mutant (right) dimers and unmodified Nap1. N (Nucleosome), T (Tetrasome), and Free DNA locations are indicated.

due to changes in the chemical environment due to increased dynamicity. In both cases, returning the samples back to room temperature led to re-appearance of the peaks corresponding to residues in the histone fold, with intensities comparable to the samples prior to heating or cooling (not shown). These results indicate that the temperature-induced peak loss observed is reversible and likely caused by changes in dynamics of the H2A/H2B dimer and not by irreversible protein aggregation. Therefore, all further experiments were conducted at 25°C.

To determine if in solution H2A/H2B folds into a similar conformation as does nucleosomal H2A/H2B, we performed secondary structure propensity (SSP) analysis on assigned residues from the *Xenopus* H2A/H2B dimer.<sup>43</sup> Comparing the SSP values to secondary structure elements found in a high-resolution crystal structure of the nucleosome (PDB 1KX5)<sup>44</sup> showed that the H2A/H2B dimer similarly folds in solution (Figures 6C and 6D, respectively). The most noticeable differences are in H2A, in which the  $\alpha$ N and two C-terminal  $3_{10}$  helices are found in the nucleosome crystal structure but are not detected in the H2A/H2B dimer in solution.<sup>38,44</sup> These elements are absent in the NMR structure of the human and *Drosophila* H2A/H2B dimer.<sup>7,8</sup> Furthermore, both the  $\alpha$ N helix and two short C-terminal  $3_{10}$  helices of H2A make direct contacts with the phosphate backbone of DNA in the structures of the nucleosome, suggesting that these helices may form either upon chaperone binding or during nucleosome formation for proper incorporation of H2A/H2B (Figure 6E). We also noted that the  $\alpha$ C of H2A appears extended in solution compared to the nucleosome structure. Unlike the  $\alpha$ N and  $3_{10}$  helices, the  $\alpha$ C helix of H2A is buried in the middle of the nucleosome structure and makes no direct contact with DNA. However, it makes multiple direct contacts with the  $\alpha$ 3 and  $\alpha$ C helices of H2B in the nucleosome structure, and extension of this helix would likely cause steric clashes with the C-termini of both H2B and H4 in the nucleosome structure. These results indicate that, while *Xenopus* H2A/H2B dimers in solution largely resemble nucleosomal H2A/H2B, they exhibit structural features that must change prior to nucleosome incorporation. To test if  $\alpha$ N and 3–10 helix stabilization is necessary for chaperone-dependent nucleosome assembly, we ran MD simulations with H2A/H2B modeled with N-terminus as a random coil. Over the course of >1  $\mu$ s trajectories, no helix formation was observed for the apo histones, but in the presence of Npm2A2glu4 and Nap1A3glu9 peptides, an increased propensity for helices and loops was observed (Figures S5H and S5I). We then compared Nap1 deposition of wildtype or H2AS18P/H2B; this S18P mutant is predicted to be helix destabilizing. Supporting the hypothesis that pre-formation of this helix is important, we observed reduced deposition of this mutant dimer (Figure 6F).

**Chemical shift perturbation (CSP) mapping of Npm2 peptide binding to the H2A/H2B dimer**

To determine consequences of chaperone acidic IDR interactions with histones in solution, we utilized chemical shift perturbation (CSP) and peak broadening (peak intensity) analysis of chaperones titrated against either [U-<sup>2</sup>H,<sup>15</sup>N]-H2A/H2B or H2A/[U-<sup>2</sup>H,<sup>15</sup>N]-H2B samples. As our prior analysis revealed that the Npm2 C-terminal Tail domain (residues 119–146) tightly bound H2A/H2B,<sup>9</sup> we first determined gross changes upon Npm2 Tail binding. Upon titration of the Tail domain the most evident change was the global loss of peak intensities for nearly all residues within the histone fold (Figure S6C). Decreased peak intensity can arise from exchange processes, conformational exchange, or rapid binding/unbinding dynamics. Surprisingly, most of these residues (25–100 for H2A, and 39–123 for H2B) decreased to ~50% of their original intensity after binding, whereas peaks corresponding to the disordered histone tails remained intense in both the bound and unbound state.

To delineate the specific histone interactions of the acidic IDRs of Npm2, we performed similar CSP experiments using the short Npm2 A2 peptide (<sup>122</sup>DYSWAEEDE<sup>131</sup>). Upon titration of this peptide into labeled histones, we observed that peaks remained at a similar intensity as in the unbound state, with most residues in the histone fold only decreasing to ~75% of their original intensities (Figure S5C, second row). CSPs were significantly smaller than with the complete Tail domain, with very few residues shifting >0.05ppm. All residues that shifted significantly upon titration of this peptide also shifted in the Tail titration experiments, indicating a similar binding site. For the [U-<sup>2</sup>H,<sup>15</sup>N]-H2A/H2B sample, significant CSPs (>0.05ppm) were observed for residues V27, G28, R29, and V100 (Figure 7A). For the H2A/[U-<sup>2</sup>H,<sup>15</sup>N]-H2B sample significant CSPs (>0.05ppm) were observed for residues I39, T119, T122 (Figure 7B). Compared to the Tail titration, there appeared to be a greater preference for the C-terminus of H2A and the N-terminus of H2B with this short peptide, possibly indicating weaker binding site specificity.

Next, to test molecular consequences of glutamylation on histone binding, we used glutamylated synthetic unmodified and glutamylated Npm2 A2 peptides. Addition of the synthetic glutamylated peptides (A2glu1, A2glu or A2glu4) to the labeled dimers exhibited a concentration dependent increase in peak broadening and CSP for almost all residues (Figures S6C and S7A–S7D). Such profound effect on the overall dynamics and conformation of the histone dimer is consistent with the stronger binding affinity of the glutamylated peptides compared to the unmodified peptide. Of note, residues in the histone fold that appeared to be actively involved in the interaction with the longer tail peptide depicted a higher degree of perturbation upon addition of the glutamylated Npm2 A2 glu4 peptide. Additionally, residues in the H2A N-terminal helices A12, A14, K13, K15, T16, G28, R29, H31, and R32 in [U-<sup>2</sup>H,<sup>15</sup>N]-H2A/H2B, also predicted by MD simulation studies to be important for interaction undergo significant changes (Figure 7C). Ligand binding often leads to conformational changes in the protein that propagates to distant regions, altering the chemical environments of nuclei that are not directly involved in binding. In line with this hypothesis, we also observed a few residues in the C-terminal helix of [U-<sup>2</sup>H,<sup>15</sup>N]-H2A/H2B namely, D90, E92, L93, and N94 depicting similar changes. In the case of H2A/[U-<sup>2</sup>H,<sup>15</sup>N]-H2B, residues I39, S123, A124, and K125 were additionally affected (residue I39 is shown in Figure 7D).

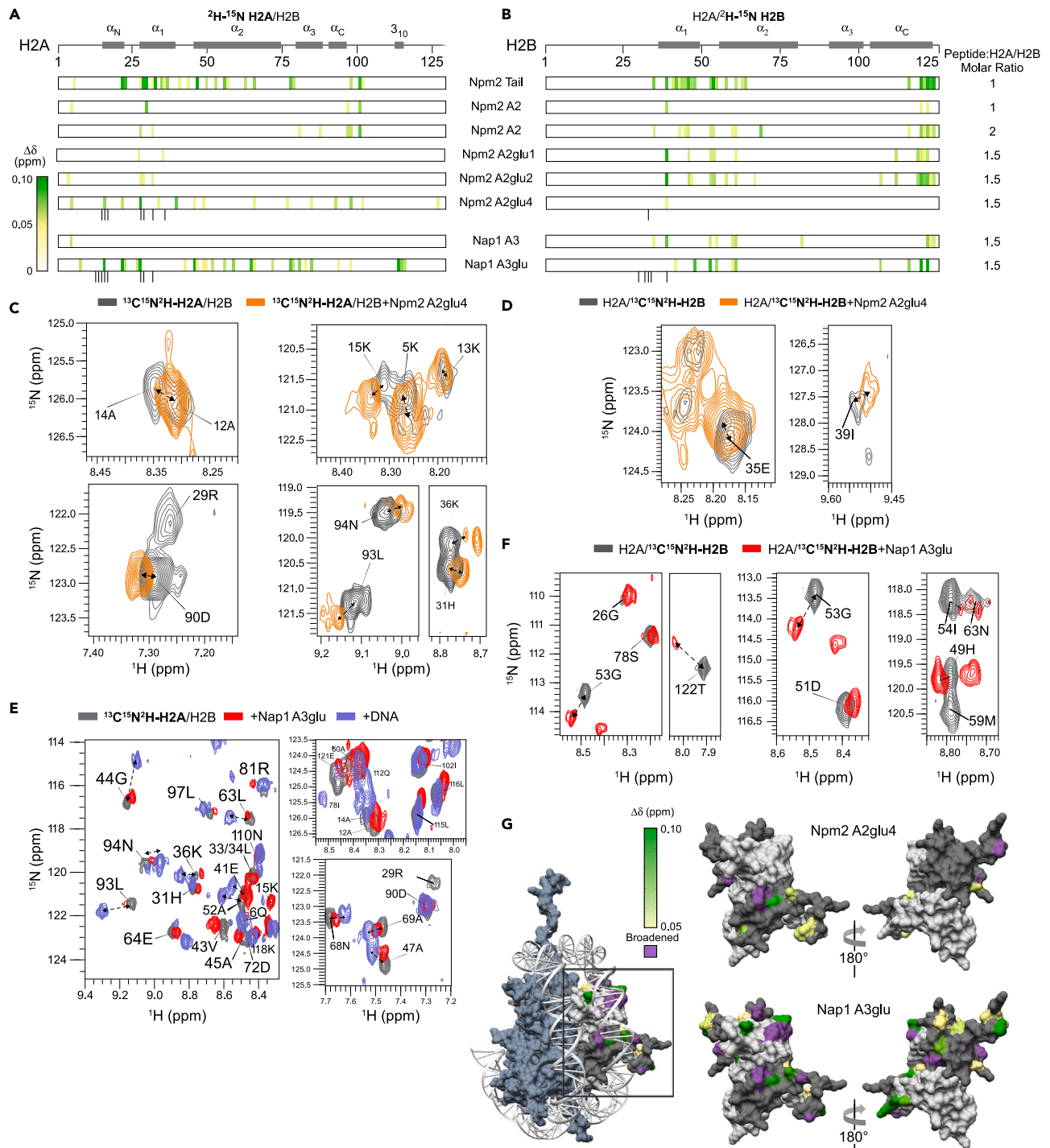


**Figure 7. Glutamylated acidic IDRs bind H2A/H2B's DNA interacting surface**

(A) Heatmap representation of indicated histone chaperone peptide induced chemical shift perturbations (CSP, scale as indicated on left index, yellow to red) across H2A assigned residues in dimer with H2B. Domain structure of H2A is shown.  
 (B) Heatmap representation of indicated histone chaperone peptide induced chemical shift perturbations (CSP, scale as indicated on left index, yellow to red) across H2B assigned residues in dimer with H2A. Domain structure of H2B is shown.  
 (C)  $^2\text{H}$ - $^{15}\text{N}$ -H2A residues (gray) undergoing CSP and/or line broadening upon Npm2 A2glu4 peptide addition (1.5X molar ratio peptide:histone, orange).  
 (D)  $^2\text{H}$ - $^{15}\text{N}$ -H2B residues (gray) undergoing CSP and/or line broadening upon Npm2 A2glu4 peptide addition (1.5X molar ratio peptide:histone, orange).

**Figure 7. Continued**

(E)  $^2\text{H}$ - $^{15}\text{N}$ -H2A residues (gray) undergoing CSP and/or line broadening upon either Nap1 A3glu peptide or DNA addition (1.5X molar ratio peptide:histone, red; DNA:histone, blue).

(F)  $^2\text{H}$ - $^{15}\text{N}$ -H2B residues (gray) undergoing CSP and/or line broadening upon Nap1 A3glu peptide addition (1.5X molar ratio peptide:histone, orange).

(G) Histone H2A (dark gray) and H2B (light gray) from the nucleosome structure shown, with CSPs (green scale) and broadened (purple) residues highlighted for both Npm2A2glu4 (top) and Nap1 A3glu (bottom) peptide.

**Chemical shift perturbation (CSP) mapping of Nap1 peptide binding to the H2A/H2B dimer**

Next, we sought to do similar binding experiments using the longer Nap1 peptide. Compared to the Npm2 tail peptide, the Nap1 peptide interacted much more strongly with the histone dimers, with almost up to 50% peak broadening for majority of the residues in both  $[\text{U}\text{-}^2\text{H}, ^{15}\text{N}]$ -H2A/H2B and H2A/ $[\text{U}\text{-}^2\text{H}, ^{15}\text{N}]$ -H2B when compared to the unbound state (Figures S7E–S7G; Tables S1–S4). Consistent with the MD simulations, this observation could be attributed to the longer peptide length providing a higher surface area of interaction. Like the Npm2 A4glu peptide interacting sites, most of these residues belonged to the histone fold region. Certain others included residues, R36, R77, L83, S113, and L116 in  $[\text{U}\text{-}^2\text{H}, ^{15}\text{N}]$ -H2A/H2B and G26, E35, K46, Q47, A58, M59, S64, and residues in the C-terminal  $3_{10}$  helix K120, and Y121 as predicted by the MD studies (Figure 7E). Compared to this, the glutamylated variant of Nap1 peptide showed greater CSP for almost all the residues in the histone fold regions. Residues like T16, H31, L65, L93, and N94 in  $[\text{U}\text{-}^2\text{H}, ^{15}\text{N}]$ -H2A/H2B and I39, T122, S123, and K125 in H2A/ $[\text{U}\text{-}^2\text{H}, ^{15}\text{N}]$ -H2B showed higher CSP and/or broadening when compared to non-glutamylated variant (Figure 7F). Finally, these conserved H2A/H2B DNA binding, chaperone peptide interacting regions were also observed on histone peptide array studies with full-length Npm2<sup>9</sup> and full-length Nap1 (Figure S7H). Overall, these observations support chaperone IDR specific and localized H2A/H2B interactions on DNA binding surfaces, greatly amplified by the presence of glutamate glutamylation.

**DISCUSSION**

Due to the lack of structural conservation, generalized histone chaperone mechanisms have long been elusive. In this work, we tested and validated the hypothesis that histone chaperone acidic IDRs act as DNA mimetics to pre-stabilize histones H2A/H2B for deposition and also to remove DNA:histone aggregates. Using biochemical analysis of the canonical—but structurally and biologically unique—*Xenopus laevis* histone chaperones Npm2 and Nap1, we directly show the mechanistic function of these acidic tails. We confirmed glutamate-glutamylation of these acidic tails enhance their function in histone binding, histone:DNA aggregate resolution, and nucleosome assembly (Figure 7G).

As would be expected from non-enzymatic transfer process, our experiments revealed that nucleosome assembly regulation by acidic IDRs is highly concentration dependent. While glutamylation promoted nucleosome assembly at lower chaperone concentrations, at higher chaperone concentrations disassembly predominated. Future studies are needed to determine the biological regulatory significance of these observations. Neither Nap1 nor Npm2, with or without glutamylation, could disassemble either histone dimers bound to DNA or pre-assembled nucleosomes. These much more stable DNA:histone complexes, with extensive molecular contacts, may require ATP-dependent remodelers, other factors, or histone modifications like acetylation to successfully disassemble. Future studies are required to determine the relative contributions of histone chaperones and ATPases in chromatin disassembly.

MD simulations and solution NMR experiments supported our biochemical findings by revealing intricate interactions that lead to increased DNA mimicry. The simulations demonstrate that glutamylation of these acidic IDRs promotes contact with H2A/H2B, resulting in increased histone fold stability. Biophysically testing these binding predictions, NMR studies revealed distinct secondary structural differences in H2A/H2B, suggesting that these chaperone peptides might interact more favorably in a nucleosome-like conformation. The NMR data show that the glutamylated regions interact at the same sites as DNA does on the histones, demonstrating that these modifications function to increase DNA mimicry. This discovery significantly broadens our understanding of post-translational modifications in mediating stabilization of H2A/H2B heterodimers and promoting chaperone efficiency.

Our NMR assignment and secondary structure analysis of the *Xenopus* H2A/H2B dimer shows that while most of the histone fold is identical to that observed in the nucleosome structure, the short N-terminal helix of H2A does not form in solution. This finding is also consistent with the NMR structural analysis of the human H2A/H2B dimer in solution.<sup>7</sup> This helix is present in every published nucleosome crystal structure and makes direct contact with the phosphate backbone of the DNA. This likely indicates that this helix must form for H2A/H2B to be properly deposited onto DNA to form nucleosomes. Consistent with a regulatory role for this region, “oncohistone” mutations have been identified in these helices. Chaperone binding may induce the formation of this helix, thus promoting the deposition of H2A/H2B onto DNA. Supporting this hypothesis, we previously detected contacts between the Npm2 Tail domain and a peptide corresponding to this N-terminal helix in peptide array experiments, and our previous PRE-NMR structural models position A2 directly adjacent to this region.<sup>9</sup> H2A S18P mutant histone dimer exhibited reduced Nap1-dependent deposition on pre-existing tetramers, consistent with formation of this helix as an essential step. We detected large CSPs adjacent to this region upon titrating both Npm2 and Nap1 peptides. Due to peak broadening and unassigned residues, we were unable to determine if this helix forms upon chaperone binding; however, these CSPs could arise via direct binding, binding induced structural changes, such as helix formation, or a combination of the two. As our MD simulations started with the nucleosome core particle structure and were of likely too short a timescale to observe helix formation, atomic resolution structures of the H2A/H2B dimer bound to Npm2 and Nap1 acidic peptides may be required to determine if this helix is present in the complex. To that end, our crystallization trials with both H2A/H2B full length dimers and our single-chain H2B-H2A crystal form<sup>45</sup> with chaperone peptides were unsuccessful.

Overall, we propose that the acidic IDRs act as dynamic scaffolds for transient, yet high-affinity interactions with histones H2A/H2B. Indeed, in our MD simulations, both the apo and glutamylated peptides approach the histone H2A/H2B surface, within ~50 ns. Highlighting its enhanced interaction and stability with the histone dimer compared to the apo peptide, the glutamylated peptide forms a more stable and specific ensemble over an extended timescale. Our observations are similar to the recent studies of extreme protein disorder in the prothymosin  $\alpha$  linker histone chaperone, which revealed its behavior as a protein polyelectrolyte.<sup>39,46</sup> Biological polyelectrolyte domains, modulated through the glutamylation of acidic disordered regions, may therefore have a unique ability to maintain highly responsive chaperone regulatory networks by altering histone affinity. This suggests that the glutamylation-driven enhancement of a polyelectrolyte state serves as a mechanism to tune the responsiveness of cellular processes. Glutamate-glutamylation may therefore enable adaptation to changing environmental signals or conditions and may be pivotal for the robustness and efficiency of cellular networks. These findings highlight the multifaceted roles of post-translational modifications and underscore the importance of further studies to explore their regulatory potential.

### Limitations of the study

A limitation of this study is that we did not test glutamylation consequences in a biological context. While testing histone chaperone glutamylation in cells is of critical importance to understanding the biological ramifications of this modification, it is experimentally challenging in that (1) core histone chaperones exhibit significant redundancy, making consequences poorly testable; (2) multiple and dense substrate glutamates (e.g., nine in the Nap1 A3 alone) make mutagenesis and outcomes complicated; (3) TTL4 has multiple cellular substrates, making knockdown consequences unclear. Due to the many intermediates and products, mononucleosome assembly assays can be challenging to interpret. The slowest migrating band in our assays is likely an aggregate of tetrasomes and H2A/H2B. As previously shown,<sup>47</sup> this observation is consistent with H2A/H2B spontaneously binding to DNA and to tetrasomes in the absence of a chaperone. This study was also primarily limited to histone H2A/H2B, and the role of chaperone acidic IDRs and their glutamylation on binding of H3/H4 and linker histones are unknown. We previously showed that the full Npm2 tail domain had 5-fold lower affinity for H3/H4 than it did for H2A/H2B.<sup>9</sup> Future studies will be necessary to explore the question of how glutamylation regulates H3/H4:chaperone interactions. Future studies on histone glutamylation in a biological consequence would be likely well-served by studying histone variant or linker histone deposition. NMR studies were limited to chemical shift perturbation and intensity measurements; while additional experiments could expand our quantitation of exchange details, they would not impact conclusions regarding glutamylated chaperone IDR DNA mimicry. Finally, while glutamylation has also been observed in mammalian histone chaperones, these studies were only performed in *Xenopus* Npm2 and Nap1.

### STAR★METHODS

Detailed methods are provided in the online version of this paper and include the following:

- KEY RESOURCES TABLE
- RESOURCE AVAILABILITY
  - Lead contact
  - Materials availability
  - Data and code availability
- EXPERIMENTAL MODEL AND STUDY PARTICIPANT DETAILS
  - *Xenopus laevis*
  - HeLa cells
- METHOD DETAILS
  - Chemical reagents, antibodies, and peptides
  - Molecular modeling and pK<sub>a</sub> prediction of glutamate and  $\gamma$ -glutamyl-glutamate
  - Cloning, expression, and purification of recombinant proteins
  - Purification of endogenous Nap1 from *Xenopus* egg extract
  - Mass spectrometry
  - Preparative chaperone glutamate-glutamylation
  - Competitive pull-down assays
  - Histone capture disaggregation assay
  - Tetrasome and mononucleosome assembly assays
  - Fluorescence binding assays
  - Protein thermal shift assays
  - Molecular dynamics simulations
  - Labeling scheme and NMR analysis of the *Xenopus* H2A/H2B dimer
  - Histone peptide arrays
- QUANTIFICATION AND STATISTICAL ANALYSIS

### SUPPLEMENTAL INFORMATION

Supplemental information can be found online at <https://doi.org/10.1016/j.isci.2024.109458>.

## ACKNOWLEDGMENTS

This work was supported by the National Institutes of Health [R01GM135614 to D.S., R01GM037537 to D.F.H., R35GM136357 and R01AI141816 to A.F., T32GM007491 and F31GM116536 to C.W.]. D.S. was also supported for this project by the Irma T. Hirsch Trust. The Bruker 600 MHz NMR instrument in the Structural NMR Resource at the Albert Einstein College of Medicine was purchased using funds from NIH award 1S10OD016305 and is supported by a Cancer Center Support Grant (P30 CA013330). The data collected at New York Structural Biology Center (NYSBC) was made possible by a grant from ORIP/NIH facility improvement grant CO6RR015495. We thank Mike Goger and Shibani Bhattacharya for their assistance and advice with NMR experiments run at the NYSBC. The 700 MHz spectrometer was purchased with funds from NIH grant S10OD018509. Data collected using the 800MHz Avance III spectrometer is supported by NIH grant S10OD016432. We are grateful to Anthony Spano and Anthony Frankfurter (Univ of Virginia) for the gift of the anti-glutamylation antibodies. We thank Michael Brenowitz for ongoing kibitzing and consultation and Sergei Khrapunov for assistance with fluorescence binding studies.

## AUTHOR CONTRIBUTIONS

B.M.L., C.W., and H.I. conceived and executed biochemistry and NMR experiments, analysis, and wrote the paper. P.N. conceived, executed, and analyzed molecular dynamics studies; A.F. supervised molecular dynamics studies. S.H. performed biochemistry experiments and analyzed results. S.C. assisted with and analyzed NMR studies; D.C. supervised and analyzed NMR studies; S.M.L. and J.S. performed mass spectrometry analysis; J.S. and D.F.H. supervised mass spectrometry studies. D.S. conceived and analyzed data, wrote the paper, and supervised this entire study. All authors read and approved the final manuscript.

To improve concision in portions of this manuscript, during the preparation of this work the authors used ChatGPT4.0. After using this tool, the authors fully reviewed and edited the content as needed and take full responsibility for the content of the publication.

## DECLARATION OF INTERESTS

The authors declare that they have no conflicts of interest with the contents of this article.

Received: September 27, 2023

Revised: January 8, 2024

Accepted: March 7, 2024

Published: March 8, 2024

## REFERENCES

- Hammond, C.M., Strømme, C.B., Huang, H., Patel, D.J., and Groth, A. (2017). Histone chaperone networks shaping chromatin function. *Nat. Rev. Mol. Cell Biol.* *18*, 141–158. <https://doi.org/10.1038/nrm.2016.159>.
- Andrews, A.J., Chen, X., Zevin, A., Stargell, L.A., and Luger, K. (2010). The histone chaperone Nap1 promotes nucleosome assembly by eliminating nonnucleosomal histone DNA interactions. *Mol. Cell* *37*, 834–842. <https://doi.org/10.1016/j.molcel.2010.01.037>.
- Andrews, A.J., Downing, G., Brown, K., Park, Y.J., and Luger, K. (2008). A thermodynamic model for Nap1-histone interactions. *J. Biol. Chem.* *283*, 32412–32418. <https://doi.org/10.1074/jbc.M805918200>.
- Zhou, K., Liu, Y., and Luger, K. (2020). Histone chaperone FACT Facilitates Chromatin Transcription: mechanistic and structural insights. *Curr. Opin. Struct. Biol.* *65*, 26–32. <https://doi.org/10.1016/j.sbi.2020.05.019>.
- Wang, T., Liu, Y., Edwards, G., Krzizike, D., Scherman, H., and Luger, K. (2018). The histone chaperone FACT modulates nucleosome structure by tethering its components. *Life Sci. Alliance* *1*, e201800107. <https://doi.org/10.26508/lsa.201800107>.
- Farnung, L., Ochmann, M., Engeholm, M., and Cramer, P. (2021). Structural basis of nucleosome transcription mediated by Chd1 and FACT. *Nat. Struct. Mol. Biol.* *28*, 382–387. <https://doi.org/10.1038/s41594-021-00578-6>.
- Moriwaki, Y., Yamane, T., Ohtomo, H., Ikeguchi, M., Kurita, J.I., Sato, M., Nagadoi, A., Shimojo, H., and Nishimura, Y. (2016). Solution structure of the isolated histone H2A-H2B heterodimer. *Sci. Rep.* *6*, 24999. <https://doi.org/10.1038/srep24999>.
- Zhang, H., Eerland, J., Horn, V., Schellevis, R., and van Ingen, H. (2021). Mapping the electrostatic potential of the nucleosome acidic patch. *Sci. Rep.* *11*, 23013. <https://doi.org/10.1038/s41598-021-02436-3>.
- Warren, C., Matsui, T., Karp, J.M., Onikubo, T., Cahill, S., Brenowitz, M., Cowburn, D., Girvin, M., and Shechter, D. (2017). Dynamic intramolecular regulation of the histone chaperone nucleoplasmin controls histone binding and release. *Nat. Commun.* *8*, 2215. <https://doi.org/10.1038/s41467-017-02308-3>.
- Warren, C., and Shechter, D. (2017). Fly Fishing for Histones: Catch and Release by Histone Chaperone Intrinsically Disordered Regions and Acidic Stretches. *J. Mol. Biol.* *429*, 2401–2426. <https://doi.org/10.1016/j.jmb.2017.06.005>.
- Hondele, M., Stuwe, T., Hassler, M., Halbach, F., Bowman, A., Zhang, E.T., Nijmeijer, B., Kotthoff, C., Rybin, V., Amlacher, S., et al. (2013). Structural basis of histone H2A-H2B recognition by the essential chaperone FACT. *Nature* *499*, 111–114. <https://doi.org/10.1038/nature12242>.
- English, C.M., Adkins, M.W., Carson, J.J., Churchill, M.E.A., and Tyler, J.K. (2006). Structural basis for the histone chaperone activity of Asf1. *Cell* *127*, 495–508.
- Corbeski, I., Dolinar, K., Wienk, H., Boelens, R., and van Ingen, H. (2018). DNA repair factor APLF acts as a H2A-H2B histone chaperone through binding its DNA interaction surface. *Nucleic Acids Res.* *46*, 7138–7152. <https://doi.org/10.1093/nar/gky507>.
- Huang, H., Stromme, C.B., Saredi, G., Hodl, M., Strandsby, A., Gonzalez-Aguilera, C., Chen, S., Groth, A., and Patel, D.J. (2015). A unique binding mode enables MCM2 to chaperone histones H3-H4 at replication forks. *Nat. Struct. Mol. Biol.* *22*, 618–626. <https://doi.org/10.1038/nsmb.3055>.
- Richet, N., Liu, D., Legrand, P., Velours, C., Corpet, A., Gaubert, A., Bakail, M., Moal-Raisin, G., Guerois, R., Compere, C., et al. (2015). Structural insight into how the human helicase subunit MCM2 may act as a histone chaperone together with ASF1 at the replication fork. *Nucleic Acids Res.* *43*, 1905–1917. <https://doi.org/10.1093/nar/gkv021>.
- Corbeski, I., Guo, X., Eckhardt, B.V., Fasci, D., Wiegant, W., Graewert, M.A., Vreeken, K., Wienk, H., Svergun, D.I., Heck, A.J.R., et al. (2022). Chaperoning of the histone octamer by the acidic domain of DNA repair factor APLF. *Sci. Adv.* *8*, eabo0517. <https://doi.org/10.1126/sciadv.abo0517>.
- D'Arcy, S., Martin, K.W., Panchenko, T., Chen, X., Bergeron, S., Stargell, L.A., Black, B.E., and Luger, K. (2013). Chaperone Nap1 shields histone surfaces used in a nucleosome and can put H2A-H2B in an unconventional tetrameric form. *Mol. Cell* *51*, 662–677. <https://doi.org/10.1016/j.molcel.2013.07.015>.
- Ohtomo, H., Yamane, T., Oda, T., Kodera, N., Kurita, J.-I., Tsunaka, Y., Amyot, R., Ikeguchi, M., and Nishimura, Y. (2023). Dynamic Solution Structures of Whole Human NAP1

- Dimer Bound to One and Two Histone H2A-H2B Heterodimers Obtained by Integrative Methods. *J. Mol. Biol.* 435, 168189. <https://doi.org/10.1016/j.jmb.2023.168189>.
19. Aguilar-Gurreri, C., Larabi, A., Vinayachandran, V., Patel, N.A., Yen, K., Reja, R., Ebong, I.O., Schoehn, G., Robinson, C.V., Pugh, B.F., and Panne, D. (2016). Structural evidence for Nap1-dependent H2A-H2B deposition and nucleosome assembly. *EMBO J.* 35, 1465–1482. <https://doi.org/10.15252/embj.201694105>.
  20. Ohtomo, H., Akashi, S., Moriwaki, Y., Okuwaki, M., Osakabe, A., Nagata, K., Kurumizaka, H., and Nishimura, Y. (2016). C-terminal acidic domain of histone chaperone human NAP1 is an efficient binding assistant for histone H2A-H2B, but not H3-H4. *Gene Cell.* 21, 252–263. <https://doi.org/10.1111/gtc.12339>.
  21. Sarkar, P., Zhang, N., Bhattacharyya, S., Salvador, K., and D'Arcy, S. (2019). Characterization of Caenorhabditis elegans Nucleosome Assembly Protein 1 Uncovers the Role of Acidic Tails in Histone Binding. *Biochemistry* 58, 108–113. <https://doi.org/10.1021/acs.biochem.8b01033>.
  22. Nagae, F., Takada, S., and Terakawa, T. (2023). Histone chaperone Nap1 dismantles an H2A/H2B dimer from a partially unwrapped nucleosome. *Nucleic Acids Res.* 51, 5351–5363. <https://doi.org/10.1093/nar/gkad396>.
  23. Mahalingam, K.K., Keith Keenan, E., Strickland, M., Li, Y., Liu, Y., Ball, H.L., Tanner, M.E., Tjandra, N., and Roll-Mecak, A. (2020). Structural basis for polyglutamate chain initiation and elongation by TTL family enzymes. *Nat. Struct. Mol. Biol.* 27, 802–813. <https://doi.org/10.1038/s41594-020-0462-0>.
  24. Rogowski, K., van Dijk, J., Magiera, M.M., Bosc, C., Deloulme, J.C., Bosson, A., Peris, L., Gold, N.D., Lacroix, B., Bosch Grau, M., et al. (2010). A family of protein-deglutamylating enzymes associated with neurodegeneration. *Cell* 143, 564–578. <https://doi.org/10.1016/j.cell.2010.10.014>.
  25. Eddé, B., Rossier, J., Le Caer, J.P., Desbryères, E., Gros, F., and Denoulet, P. (1990). Posttranslational glutamylation of alpha-tubulin. *Science* 247, 83–85.
  26. Redeker, V., Melki, R., Promé, D., Le Caer, J.P., and Rossier, J. (1992). Structure of tubulin C-terminal domain obtained by subtilisin treatment. The major alpha and beta tubulin isoforms from pig brain are glutamylated. *FEBS Lett.* 313, 185–192. [https://doi.org/10.1016/0014-5793\(92\)81441-n](https://doi.org/10.1016/0014-5793(92)81441-n).
  27. Audebert, S., Desbryères, E., Gruszczynski, C., Koulakoff, A., Gros, F., Denoulet, P., and Eddé, B. (1993). Reversible polyglutamylation of alpha- and beta-tubulin and microtubule dynamics in mouse brain neurons. *Mol. Biol. Cell* 4, 615–626. <https://doi.org/10.1091/mbc.4.6.615>.
  28. Yu, I., Garnham, C.P., and Roll-Mecak, A. (2015). Writing and Reading the Tubulin Code. *J. Biol. Chem.* 290, 17163–17172. <https://doi.org/10.1074/jbc.R115.637447>.
  29. Chick, J.M., Kolippakkam, D., Nusinow, D.P., Zhai, B., Rad, R., Huttlin, E.L., and Gygi, S.P. (2015). A mass-tolerant database search identifies a large proportion of unassigned spectra in shotgun proteomics as modified peptides. *Nat. Biotechnol.* 33, 743–749. <https://doi.org/10.1038/nbt.3267>.
  30. Onikubo, T., Nicklay, J.J., Xing, L., Warren, C., Anson, B., Wang, W.L., Burgos, E.S., Ruff, S.E., Shabanowitz, J., Cheng, R.H., et al. (2015). Developmentally Regulated Post-translational Modification of Nucleoplasmic Controls Histone Sequestration and Deposition. *Cell Rep.* 10, 1735–1748. <https://doi.org/10.1016/j.celrep.2015.02.038>.
  31. Miller, K.E., and Heald, R. (2015). Glutamylation of Nap1 modulates histone H1 dynamics and chromosome condensation in *Xenopus*. *J. Cell Biol.* 209, 211–220. <https://doi.org/10.1083/jcb.201412097>.
  32. Regnard, C., Desbryères, E., Huet, J.C., Beauvallet, C., Pernellet, J.C., and Eddé, B. (2000). Polyglutamylation of nucleosome assembly proteins. *J. Biol. Chem.* 275, 15969–15976. <https://doi.org/10.1074/jbc.M000045200>.
  33. van Dijk, J., Miro, J., Strub, J.M., Lacroix, B., van Dorselaer, A., Edde, B., and Janke, C. (2008). Polyglutamylation is a post-translational modification with a broad range of substrates. *J. Biol. Chem.* 283, 3915–3922. <https://doi.org/10.1074/jbc.M705813200>.
  34. Kashiwaya, K., Nakagawa, H., Hosokawa, M., Mochizuki, Y., Ueda, K., Piao, L., Chung, S., Hamamoto, R., Eguchi, H., Ohigashi, H., et al. (2010). Involvement of the tubulin tyrosine ligase-like family member 4 polyglutamylase in PELP1 polyglutamylation and chromatin remodeling in pancreatic cancer cells. *Cancer Res.* 70, 4024–4033. <https://doi.org/10.1158/0008-5472.can-09-4444>.
  35. Liu, W.H., and Churchill, M.E.A. (2012). Histone transfer among chaperones. *Biochem. Soc. Trans.* 40, 357–363. <https://doi.org/10.1042/bst20110737>.
  36. Elsässer, S.J., and D'Arcy, S. (2013). Towards a mechanism for histone chaperones. *Biochim. Biophys. Acta* 1819, 211–221. <https://doi.org/10.1016/j.bbaggm.2011.07.007>.
  37. Huang, Y., Dai, Y., and Zhou, Z. (2020). Mechanistic and structural insights into histone H2A-H2B chaperone in chromatin regulation. *Biochem. J.* 477, 3367–3386. <https://doi.org/10.1042/BCJ20190852>.
  38. Luger, K., Mäder, A.W., Richmond, R.K., Sargent, D.F., and Richmond, T.J. (1997). Crystal structure of the nucleosome core particle at 2.8 Å resolution. *Nature* 389, 251–260.
  39. Heidarsson, P.O., Mercadante, D., Sottini, A., Nettels, D., Borgia, M.B., Borgia, A., Kilic, S., Fierz, B., Best, R.B., and Schuler, B. (2022). Release of linker histone from the nucleosome driven by polyelectrolyte competition with a disordered protein. *Nat. Chem.* 14, 224–231. <https://doi.org/10.1038/s41557-021-00839-3>.
  40. Borgia, A., Borgia, M.B., Bugge, K., Kissling, V.M., Heidarsson, P.O., Fernandes, C.B., Sottini, A., Soranno, A., Buholzer, K.J., Nettels, D., et al. (2018). Extreme disorder in an ultrahigh-affinity protein complex. *Nature* 555, 61–66. <https://doi.org/10.1038/nature25762>.
  41. Müller-Späth, S., Soranno, A., Hirschfeld, V., Hofmann, H., Rügger, S., Reymond, L., Nettels, D., and Schuler, B. (2010). From the Cover: Charge interactions can dominate the dimensions of intrinsically disordered proteins. *Proc. Natl. Acad. Sci. USA* 107, 14609–14614. <https://doi.org/10.1073/pnas.1001743107>.
  42. Sueoka, T., Hayashi, G., and Okamoto, A. (2017). Regulation of the Stability of the Histone H2A-H2B Dimer by H2A Tyr57 Phosphorylation. *Biochemistry* 56, 4767–4772. <https://doi.org/10.1021/acs.biochem.7b00504>.
  43. Marsh, J.A., Singh, V.K., Jia, Z., and Forman-Kay, J.D. (2006). Sensitivity of secondary structure propensities to sequence differences between alpha- and gamma-synuclein: implications for fibrillation. *Protein Sci.* 15, 2795–2804. <https://doi.org/10.1110/ps.062465306>.
  44. Davey, C.A., Sargent, D.F., Luger, K., Maeder, A.W., and Richmond, T.J. (2002). Solvent mediated interactions in the structure of the nucleosome core particle at 1.9 Å resolution. *J. Mol. Biol.* 319, 1097–1113.
  45. Warren, C., Bonanno, J.B., Almo, S.C., and Shechter, D. (2020). Structure of a single-chain H2A/H2B dimer. *Acta Crystallogr. F Struct. Biol. Commun.* 76, 194–198. <https://doi.org/10.1107/S2053230X20004604>.
  46. Sottini, A., Borgia, A., Borgia, M.B., Bugge, K., Nettels, D., Chowdhury, A., Heidarsson, P.O., Zosel, F., Best, R.B., Kragelund, B.B., and Schuler, B. (2020). Polyelectrolyte interactions enable rapid association and dissociation in high-affinity disordered protein complexes. *Nat. Commun.* 11, 5736. <https://doi.org/10.1038/s41467-020-18859-x>.
  47. Mattioli, F., Gu, Y., and Luger, K. (2018). Measuring Nucleosome Assembly Activity *in vitro* with the Nucleosome Assembly and Quantification (NAQ) Assay. *Bio. Protoc.* 8, e2714. <https://doi.org/10.21769/BioProtoc.2714>.
  48. Spano, A.J., and Frankfurter, A. (2010). Characterization of anti-beta-tubulin antibodies. In *Methods Cell Biol* (Elsevier Inc), pp. 33–46. [https://doi.org/10.1016/s0091-679x\(10\)95003-6](https://doi.org/10.1016/s0091-679x(10)95003-6).
  49. Delaglio, F., Grzesiek, S., Vuister, G.W., Zhu, G., Pfeifer, J., and Bax, A. (1995). NMRPipe: A multidimensional spectral processing system based on UNIX pipes. *J. Biomol. NMR* 6, 277–293. <https://doi.org/10.1007/BF00197809>.
  50. Vranken, W.F., Boucher, W., Stevens, T.J., Fogh, R.H., Pajon, A., Llinas, M., Ulrich, E.L., Markley, J.L., Ionides, J., and Laue, E.D. (2005). The CCPN data model for NMR spectroscopy: Development of a software pipeline. *Proteins* 59, 687–696. <https://doi.org/10.1002/prot.20449>.
  51. Maciejewski, M.W., Schuyler, A.D., Gryk, M.R., Moraru, I.I., Romero, P.R., Ulrich, E.L., Eghbalnia, H.R., Livny, M., Delaglio, F., and Hoch, J.C. (2017). NMRbox: A Resource for Biomolecular NMR Computation. *Biophys. J.* 112, 1529–1534. <https://doi.org/10.1016/j.bpj.2017.03.011>.
  52. Bahrami, A., Assadi, A.H., Markley, J.L., and Eghbalnia, H.R. (2009). Probabilistic Interaction Network of Evidence Algorithm and its Application to Complete Labeling of Peak Lists from Protein NMR Spectroscopy. *PLoS Comput. Biol.* 5, e1000307. <https://doi.org/10.1371/journal.pcbi.1000307>.
  53. Lee, P.-H., Huang, X.X., Teh, B.T., and Ng, L.-M. (2019). TSA-CRAFT: A Free Software for Automatic and Robust Thermal Shift Assay Data Analysis. *SLAS Discov.* 24, 606–612. <https://doi.org/10.1177/2472555218823547>.
  54. Case, D.A., Aktulga, H.M., Belfon, K., Cerutti, D.S., Cisneros, G.A., Cruzeiro, V.W.D., Forouzan, N., Giese, T.J., Götz, A.W., Gohlke, H., et al. (2023). AmberTools. *J. Chem. Inf. Model.* 63, 6183–6191. <https://doi.org/10.1021/acs.jcim.3c01153>.
  55. Schrödinger, L.L.C. (2015). The PyMOL Molecular Graphics System, Version 1.8.
  56. Anandakrishnan, R., Aguilari, B., and Onufriev, A.V. (2012). H++ 3.0: automating pK prediction and the preparation of

- biomolecular structures for atomistic molecular modeling and simulations. *Nucleic Acids Res.* 40, W537–W541. <https://doi.org/10.1093/nar/gks375>.
57. Schindelin, J., Arganda-Carreras, I., Frise, E., Kaynig, V., Longair, M., Pietzsch, T., Preibisch, S., Rueden, C., Saalfeld, S., Schmid, B., et al. (2012). Fiji: an open-source platform for biological-image analysis. *Nat. Methods* 9, 676–682. <https://doi.org/10.1038/nmeth.2019>.
  58. UniProt Consortium (2023). UniProt: the Universal Protein Knowledgebase in 2023. *Nucleic Acids Res.* 51, D523–D531. <https://doi.org/10.1093/nar/gkac1052>.
  59. Spano, A.J., and Frankfurter, A. (2010). Characterization of anti-beta-tubulin antibodies. *Methods Cell Biol.* 95, 33–46. [https://doi.org/10.1016/s0091-679x\(10\)95003-6](https://doi.org/10.1016/s0091-679x(10)95003-6).
  60. Lorton, B.M., Harijan, R.K., Burgos, E.S., Bonanno, J.B., Almo, S.C., and Shechter, D. (2020). A Binary Arginine Methylation Switch on Histone H3 Arginine 2 Regulates Its Interaction with WDR5. *Biochemistry* 59, 3696–3708. <https://doi.org/10.1021/acs.biochem.0c00035>.
  61. Aslanidis, C., and de Jong, P.J. (1990). Ligation-independent cloning of PCR products (LIC-PCR). *Nucleic Acids Res.* 18, 6069–6074. <https://doi.org/10.1093/nar/18.20.6069>.
  62. Banaszynski, L.A., Allis, C.D., and Shechter, D. (2010). Analysis of histones and chromatin in *Xenopus laevis* egg and oocyte extracts. *Methods* 51, 3–10. <https://doi.org/10.1016/j.ymeth.2009.12.014>.
  63. Luger, K., Rechsteiner, T.J., and Richmond, T.J. (1999). Expression and purification of recombinant histones and nucleosome reconstitution. *Methods Mol. Biol.* 119, 1–16.
  64. Lowary, P.T., and Widom, J. (1998). New DNA sequence rules for high affinity binding to histone octamer and sequence-directed nucleosome positioning. *J. Mol. Biol.* 276, 19–42. <https://doi.org/10.1006/jmbi.1997.1494>.
  65. Lee, P.H., Huang, X.X., Teh, B.T., and Ng, L.M. (2019). TSA-CRAFT: A Free Software for Automatic and Robust Thermal Shift Assay Data Analysis. *SLAS Discov.* 24, 606–612. <https://doi.org/10.1177/2472555218823547>.
  66. Salomón-Ferrer, R., Case, D.A., and Walker, R.C. (2012). An overview of the amber biomolecular simulation package. *WIREs Comput. Mol. Sci.* 3, 198–210. <https://doi.org/10.1002/wcms.1121>.
  67. Case, D.A., Belfon, K., Ben-Shalom, I.Y., Brozell, S.R., Cerutti, D.S., Cheatham, T.E., III, Cruzeiro, V.W.D., Darden, T.A., Duke, R.E., Giambasu, G., et al. (2020). AMBER 2020 (University of California).
  68. Roe, D.R., and Cheatham, T.E., 3rd (2013). PTRAJ and CPPTRAJ: Software for Processing and Analysis of Molecular Dynamics Trajectory Data. *J. Chem. Theory Comput.* 9, 3084–3095. <https://doi.org/10.1021/ct400341p>.
  69. Grudman, S., Fajardo, J.E., and Fiser, A. (2022). INTERCAAT: identifying interface residues between macromolecules. *Bioinformatics* 38, 554–555. <https://doi.org/10.1093/bioinformatics/btab596>.
  70. Schubert, E., Sander, J., Ester, M., Kriegel, H.P., and Xu, X. (2017). DBSCAN Revisited, Revisited: Why and How You Should (Still) Use DBSCAN. *ACM Trans. Database Syst.* 42, 1–21.
  71. Marley, J., Lu, M., and Bracken, C. (2001). A method for efficient isotopic labeling of recombinant proteins. *J. Biomol. NMR* 20, 71–75. <https://doi.org/10.1023/a:1011254402785>.
  72. Rovnyak, D., Frueh, D.P., Sastry, M., Sun, Z.Y.J., Stern, A.S., Hoch, J.C., and Wagner, G. (2004). Accelerated acquisition of high resolution triple-resonance spectra using non-uniform sampling and maximum entropy reconstruction. *J. Magn. Reson.* 170, 15–21. <https://doi.org/10.1016/j.jmr.2004.05.016>.
  73. Vranken, W.F., Boucher, W., Stevens, T.J., Fogh, R.H., Pajon, A., Llinas, M., Ulrich, E.L., Markley, J.L., Ionides, J., and Laue, E.D. (2005). The CCPN data model for NMR spectroscopy: development of a software pipeline. *Proteins* 59, 687–696. <https://doi.org/10.1002/prot.20449>.
  74. Bahrami, A., Assadi, A.H., Markley, J.L., and Eghbalnia, H.R. (2009). Probabilistic interaction network of evidence algorithm and its application to complete labeling of peak lists from protein NMR spectroscopy. *PLoS Comput. Biol.* 5, e1000307. <https://doi.org/10.1371/journal.pcbi.1000307>.

STAR★METHODS

KEY RESOURCES TABLE

REAGENT or RESOURCE	SOURCE	IDENTIFIER
<b>Antibodies</b>		
Anti-Npm2 (full length)	This manuscript	N/A
Anti-Npm2 (core)	This manuscript	N/A
Anti-Nap1	This manuscript	N/A
Anti-mono-glutamylated (TTβIIIglu)	Spano and Frankfurter <sup>48</sup>	<a href="https://doi.org/10.1016/s0091-679x(10)95003-6">https://doi.org/10.1016/s0091-679x(10)95003-6</a>
<b>Bacterial and virus strains</b>		
<i>Escherichia coli</i> DH5 alpha	Homemade	N/A
<i>Escherichia coli</i> Rosetta 2	Homemade	Novagen/EMD Millipore 71402
<b>Chemicals, peptides, and recombinant proteins</b>		
Npm2 A2 peptides (unmodified and mono-glutamylated)	GenScript Custom Synthesis	<a href="http://www.genscript.com">www.genscript.com</a>
Npm2 (119-146aa)	Warren et al. <sup>9</sup>	<a href="https://doi.org/10.1038/s41467-017-02308-3">https://doi.org/10.1038/s41467-017-02308-3</a>
Nap1 (350-382aa)	This manuscript	N/A
Tobacco Etch Virus protease	Homemade	RRID:Addgene 8827
Guanidine hydrochloride	GoldBio	Cat#G-211-5
Histone peptide array	JPT Peptide Technologies	Cat# His_MA_01
Sequencing grade modified Endoproteinase Trypsin	Promega Corporation	<a href="https://www.promega.com/products/mass-spectrometry/trypsin/sequencing-grade-modified-trypsin/?catNum=V5111">https://www.promega.com/products/mass-spectrometry/trypsin/sequencing-grade-modified-trypsin/?catNum=V5111</a>
Sequencing grade modified Endoproteinase Arg-C	Promega Corporation	<a href="https://www.promega.com/products/mass-spectrometry/proteases-and-surfactants/arg_c-sequencing-grade/?catNum=V1881">https://www.promega.com/products/mass-spectrometry/proteases-and-surfactants/arg_c-sequencing-grade/?catNum=V1881</a>
Pierce Peptide Retention Time Calibration Mixture	Thermo Fisher Scientific	<a href="https://www.thermofisher.com/order/catalog/product/88321">https://www.thermofisher.com/order/catalog/product/88321</a>
Formic Acid, LC-MS Grade	Thermo Fisher Scientific	<a href="https://www.thermofisher.com/order/catalog/product/85178?SID=srch-srp-85178">https://www.thermofisher.com/order/catalog/product/85178?SID=srch-srp-85178</a>
Pierce Water, LC-MS Grade	Thermo Fisher Scientific	<a href="https://www.thermofisher.com/order/catalog/product/85189?SID=srch-srp-85189">https://www.thermofisher.com/order/catalog/product/85189?SID=srch-srp-85189</a>
Ammonium Bicarbonate	Sigma Aldrich	<a href="https://www.sigmaaldrich.com/US/en/substance/ammoniumbicarbonate79061066337">https://www.sigmaaldrich.com/US/en/substance/ammoniumbicarbonate79061066337</a>
Urea	Sigma Aldrich	<a href="https://www.sigmaaldrich.com/US/en/substance/600657136">https://www.sigmaaldrich.com/US/en/substance/600657136</a>
Dithiothreitol	Sigma Aldrich	<a href="https://www.sigmaaldrich.com/US/en/substance/dldithiothreitol154253483123">https://www.sigmaaldrich.com/US/en/substance/dldithiothreitol154253483123</a>
Iodoacetamide	Sigma Aldrich	<a href="https://www.sigmaaldrich.com/US/en/product/sigma/i1149">https://www.sigmaaldrich.com/US/en/product/sigma/i1149</a>
Glacial Acetic Acid, >99.9% purity	Sigma Aldrich	<a href="https://www.sigmaaldrich.com/US/en/substance/aceticacidglacial100600564197">https://www.sigmaaldrich.com/US/en/substance/aceticacidglacial100600564197</a>
Burdick and Jackson Acetonitrile, LC-MS grade	Honeywell	<a href="https://lab.honeywell.com/shop/acetonitrile-lc015">https://lab.honeywell.com/shop/acetonitrile-lc015</a>
<b>Critical commercial assays</b>		
Phusion High-Fidelity PCR Kit	New England Biolabs	E0553L
NucleoSpin Gel and PCR Clean-Up Kit	Takara Bio	Cat#740611.50

(Continued on next page)

**Continued**

REAGENT or RESOURCE	SOURCE	IDENTIFIER
<b>Deposited data</b>		
H2A and H2B NMR chemical shifts in the <i>Xenopus</i> H2A/H2B heterodimer	This manuscript	BMRB: 52244; <a href="https://bmr.io/data_library/summary/index.php?bmrld=52244">https://bmr.io/data_library/summary/index.php?bmrld=52244</a>
<b>Experimental models: Cell lines</b>		
HeLa cells	ATCC	RRID:CVCL_0030
<b>Experimental models: Organisms/strains</b>		
<i>Xenopus laevis</i>	eNasco	RRID:NCBITaxon_8355
<b>Oligonucleotides</b>		
32bp DNA oligo (+ strand): TTT CCA AAT ACA CTT TTG GTA GAA TCT GCA GG	Integrated DNA Technologies Custom Synthesis	<a href="http://www.idtdna.com">www.idtdna.com</a>
32bp DNA oligo (- strand): CCT GCA GAT TCT ACC AAA AGT GTA TTT GGA AA	Integrated DNA Technologies Custom Synthesis	<a href="http://www.idtdna.com">www.idtdna.com</a>
187bp DNA forward primer: GGTCGCTGTCAATACATGC	Integrated DNA Technologies Custom Synthesis	<a href="http://www.idtdna.com">www.idtdna.com</a>
187bp DNA reverse primer: GGACCCTATACGCGGC	Integrated DNA Technologies Custom Synthesis	<a href="http://www.idtdna.com">www.idtdna.com</a>
<b>Recombinant DNA</b>		
187bp DNA (PCR product)	This manuscript	Addgene plasmid PGEM-3z/601 (#26656)
<b>Software and algorithms</b>		
TOPSPIN	Bruker Corporation	<a href="https://www.bruker.com/en/products-and-solutions/mr/nmr-software/topspin.html">https://www.bruker.com/en/products-and-solutions/mr/nmr-software/topspin.html</a>
NMRPipe	Delaglio et al. <sup>49</sup>	<a href="https://doi.org/10.1007/BF00197809">https://doi.org/10.1007/BF00197809</a>
CcpNMR	Vranken et al. <sup>50</sup>	<a href="https://doi.org/10.1002/prot.20449">https://doi.org/10.1002/prot.20449</a>
NMRbox	Maciejewski et al. <sup>51</sup>	<a href="https://doi.org/10.1016/j.bpj.2017.03.01">https://doi.org/10.1016/j.bpj.2017.03.01</a>
PINE	Bahrami et al. <sup>52</sup>	<a href="https://doi.org/10.1371/journal.pcbi.1000307">https://doi.org/10.1371/journal.pcbi.1000307</a>
Maestro	Schrödinger LLC	<a href="https://newsite.schrodinger.com/">https://newsite.schrodinger.com/</a>
Chimera	UCSF	<a href="https://www.cgl.ucsf.edu/chimera/">https://www.cgl.ucsf.edu/chimera/</a>
ChemDraw 20.1.1	Revvity Signals	<a href="https://revvitysignals.com/products/research/chemdraw">https://revvitysignals.com/products/research/chemdraw</a>
Prism 10	GraphPad Software	<a href="https://www.graphpad.com/scientific-software/prism/">https://www.graphpad.com/scientific-software/prism/</a>
TSA-CRAFT	Lee et al. <sup>53</sup>	<a href="https://doi.org/10.1177/2472555218823547">https://doi.org/10.1177/2472555218823547</a>
AMBER20	Case et al. <sup>54</sup>	<a href="https://ambermd.org">https://ambermd.org</a>
PYMOL	Schrodinger LLC <sup>55</sup>	<a href="https://pymol.org/2/">https://pymol.org/2/</a>
H++ Server	Anandakrishnan et al. <sup>56</sup>	<a href="http://newbiophysics.cs.vt.edu/H++/">http://newbiophysics.cs.vt.edu/H++/</a>
FIJI	Schindelin et al. <sup>57</sup>	<a href="https://fiji.sc/">https://fiji.sc/</a>
<b>Other</b>		
Strep-Tactin Sepharose	IBA Lifesciences	Cat# 2-1201-010
Agilent 1100 series HPLC	Agilent Technologies	<a href="https://www.agilent.com/en/products/liquid-chromatography">https://www.agilent.com/en/products/liquid-chromatography</a>
Poroshell 300SB-C18 resin, 5 $\mu$ m, 300 Å	Agilent Technologies	<a href="https://www.agilent.com/en/product/biopharma-hplc-analysis/intact-subunit-analysis/poroshell-300">https://www.agilent.com/en/product/biopharma-hplc-analysis/intact-subunit-analysis/poroshell-300</a>
Sutter P-2000 microcapillary laser puller	Sutter Instrument Co.	<a href="https://www.sutter.com/MICROPIPETTE/p-2000.html">https://www.sutter.com/MICROPIPETTE/p-2000.html</a>
Polymicro Technologies polyimide coated fused silica capillary	Molex	<a href="https://www.molex.com/en-us/products/capillary-tubing">https://www.molex.com/en-us/products/capillary-tubing</a>
Kasil – Potassium silicate solution	PQ Corporation	<a href="https://www.pqcorp.com/products/">https://www.pqcorp.com/products/</a>

(Continued on next page)

**Continued**

REAGENT or RESOURCE	SOURCE	IDENTIFIER
Reprosil-Pur 120 Å C18-AQ, 3 µm and 5 µm	Dr. Maitsch GmbH	<a href="https://dr-maisch.com/dr-maisch-phases/reprosil-pur/reprosil-pur-120-c18-aq">https://dr-maisch.com/dr-maisch-phases/reprosil-pur/reprosil-pur-120-c18-aq</a>
Thermo Orbitrap™ Fusion™ Mass Spectrometer	Thermo Fisher Scientific	<a href="https://www.thermofisher.com/lcms/orbitrap.html">https://www.thermofisher.com/lcms/orbitrap.html</a>
<i>Xenopus laevis</i> Nap1 protein sequence	Uniprot Consortium <sup>58</sup>	Uniprot Q4U0Y4-2
<i>Xenopus laevis</i> Npm2 protein sequence	Uniprot Consortium <sup>58</sup>	Uniprot A0A1L8GRP4
<i>Homo sapiens</i> TTL4 protein sequence	Uniprot Consortium <sup>58</sup>	Uniprot Q14679
<i>Xenopus laevis</i> H2A protein sequence	Uniprot Consortium <sup>58</sup>	Uniprot P06897
<i>Xenopus laevis</i> H2B protein sequence	Uniprot Consortium <sup>58</sup>	Uniprot P02281

**RESOURCE AVAILABILITY****Lead contact**

Further information and requests for resources and reagents should be directed to and will be fulfilled by the Lead Contact, David Shechter ([david.shechter@einsteinmed.edu](mailto:david.shechter@einsteinmed.edu)).

**Materials availability**

All Npm2 expression clones were previously described by us.<sup>9</sup> Npm2, Nap1, and TTL4 clones and all resources will be made available upon request.

**Data and code availability**

- H2A and H2B NMR chemical shifts in the *Xenopus laevis* H2A/H2B heterodimer are available from the Biological Magnetic Resonance Data Bank (BMRB).
- All data will be made available upon request.
- No new code was generated for this study.
- Any additional information required to reanalyze the data reported in this paper is available from the [lead contact](#) upon request.

**EXPERIMENTAL MODEL AND STUDY PARTICIPANT DETAILS*****Xenopus laevis***

Sexually mature adult (greater than 1 year old) female African clawed frogs obtained from Nasco. Institutional Permission: Frogs were handled according to Albert Einstein College of Medicine IACUC-approved Protocol 00001537.

**HeLa cells**

Human cell line obtained from C. David Allis. As they were only used to purify histones, for this study these cells were not authenticated.

**METHOD DETAILS****Chemical reagents, antibodies, and peptides**

All chemical reagents were procured from Thermo Fisher Scientific (Waltham, MA), Sigma-Aldrich (St. Louis, MO), Research Products International (Mount Prospect, IL), Cambridge Isotopes Laboratory (Andover, MA), IBA Lifesciences (Göttingen, Germany), or Gold Biotechnology (Olivette, MO). The antibodies against *Xenopus laevis* Npm2 and Npm2 core domain were generated by Lampire Biological Laboratories (Pipersville, PA), using recombinant Npm2 full-length and core domain truncation antigens, respectively. The antibody against *Xenopus laevis* Nap1 was generated by Lampire Biological Laboratories (Pipersville, PA), using recombinant Nap1 antigen. The anti-monoglutamylation antibody TTβIIIglu (referred to here as anti-glu) was generously provided by Dr. Anthony Spano and Dr. Anthony Frankfurter.<sup>59</sup> Synthetic peptides corresponding to Npm2 A2 and glutamylated counterparts were obtained from GenScript (Piscataway, NJ). The Npm2 119-146aa peptide was purified as previously described.<sup>9</sup> The cDNA sequence corresponding to Nap1 350-382aa peptide containing the A3 acidic patch was cloned into the pRUTH5-GST vector which produced the peptide fused to a TEV-cleavable N-terminal His<sub>6</sub>+GST tag; expression and purification of the fused peptide is as described below for Nap1 proteins. Following cleavage of the peptide, the His<sub>6</sub>+GST tag and TEV protease were removed by subtractive Ni-NTA chromatography. The Nap1 peptide was lyophilized and further purified by reverse-phase high-performance liquid chromatography using a 250 x 10 mm 4mm Synergi Fusion-RP 80Å C12 column (Phenomenex, Torrance, CA), as previously described.<sup>60</sup>

### Molecular modeling and pK<sub>a</sub> prediction of glutamate and $\gamma$ -glutamyl-glutamate

Maestro (Shrödinger) was used to model electrostatic potential surface maps and predict pK<sub>a</sub> values for glutamate and  $\gamma$ -glutamyl-glutamate. First a glutamate molecule was modeled using the software's "Build" feature by selecting Add Fragments > Amino acids > Glu. To model  $\gamma$ -glutamyl-glutamate, another glutamate was modeled and the backbone NH<sub>2</sub> group was deleted; the terminal OH group of the initial glutamate was changed to an NH<sub>2</sub> group then this NH<sub>2</sub> group and the C $\alpha$  of the second glutamate were highlighted; right-clicking and selecting "Add bond" joined the molecules. Molecules were relaxed by clicking Edit > Minimize > All atoms. The "Poisson-Blotzmann ESP" task was used to generate electronic maps of the unmodified and modified sidechains. Electrostatic potentials are displayed from  $-10$  to  $10 k_B T/e$  [ $k_B$ , Boltzmann constant; T, temperature (kelvin); e, electron charge]. Surface transparencies were set to 30% front and 10% back from the "Surface display options" menu. pK<sub>a</sub> values were predicted using Epik by selecting the "Empirical pK<sub>a</sub>" task.

### Cloning, expression, and purification of recombinant proteins

Histones used in this study were purified and refolded as previously described.<sup>9</sup> T116 of H2B in pRUTH5-X/H2B was mutated to cysteine and purified as described for wildtype H2B. The labeling of H2B at this site was previously used for affinity measurement of Nap1 to H2A-H2B.<sup>3</sup> Purified H2BT116C was buffer exchanged to 20mM Tris pH 7.5, 2M NaCl, 1 mM EDTA, and 0.2 mM TCEP and then mixed with an equimolar amount of Alexa488-maleimide (Invitrogen) and incubated at 4°C for four hours. Then another equimolar amount of the dye was added and incubated at 4°C overnight. The conjugation reaction was terminated by addition of  $\beta$ -mercaptoethanol. The fluorescently labeled H2B-T116 was dimerized with H2A by mixing with an equimolar amount of H2A in the denaturing buffer and the dimer formed as described above. The excess dye was removed through extensive dialysis and Superdex-75 chromatography during the dimerization procedure. The concentration of the labeled dimer was measured by absorbance at 495nm. The concentration of the total histone dimers was measured by the absorbance at 280nm with a correction for the absorption by the dyes as per the supplier's instruction (Invitrogen).

Npm2 proteins were purified as previously described.<sup>30</sup> cDNA sequences corresponding to *Xenopus laevis* Nap1L.1L isoform X2 (Nap1) constructs used in this study were cloned into pRUTH5 expression vectors using ligation independent cloning,<sup>61</sup> which resulted in fusion proteins containing an N-terminal His<sub>6</sub> affinity tag followed by a Tobacco Etch Virus (TEV) protease site. The cDNA sequence corresponding to the catalytic domain of human Tubulin Tyrosine Like Ligase 4 (TTL4, 561-1199aa) was similarly cloned in to pRUTH5-GST expression vector, resulting in a protein fused to a cleavable N-terminal His<sub>6</sub>+GST tag. TTL4 catalytic domain was only soluble if the His<sub>6</sub>+GST tag remained fused to the protein. Npm2 and Nap1 proteins were expressed in Rosetta2 (DE3) *E. coli* grown in LB medium containing appropriate antibiotics to OD<sub>600</sub> ~0.7 at 37°C with agitation before induction with 0.5mM IPTG followed by 18 h incubation at 30°C with agitation. Cells were pelleted by centrifugation for 20 min at 4000  $\times$  g and resuspended at a 1:10 mass (g) to volume (mL) in lysis buffer (50 mM Tris-HCl pH 8.0, 1 M NaCl, 5 mM  $\beta$ -ME, 5 mM imidazole, 10% glycerol). Lysis was performed using an Emulsiflex C3 homogenizer (Avestin) at 4°C with two passages at approximately 12,000psi. The lysate was centrifuged at 14,000  $\times$  g for 45 min and the soluble fraction was incubated with 1 mL HisPur Ni-NTA resin (Thermo) per 1 L of cell culture at 4°C with agitation for 1 h. Ni-NTA gravity-flow columns were packed in disposable chromatography columns (Bio-Rad) and washed extensively with 25-50 column volumes (CVs) of lysis buffer, followed by 25CVs of the same buffer containing 30mM imidazole; proteins were eluted with 3CVs of the same buffer containing 300mM imidazole. Eluate containing Npm2 or Nap1 protein was transferred to dialysis tubing (10,000 MWCO) and the N-terminal His<sub>6</sub> affinity tag was cleaved by adding 6  $\times$  -histidine-tobacco etch virus (TEV) protease catalytic domain at a 1:50 mass ratio (TEV:Nap1) then dialyzed for 16 h at 4°C against buffer containing 50 mM Tris-HCl pH 8.0, 150 mM NaCl, 5 mM  $\beta$ -ME, and 10% glycerol. Subtractive Ni-NTA chromatography was then performed to remove the affinity tag and TEV protease. Proteins were concentrated to ~15 mg/mL and polished by size exclusion chromatography (Superose 6 Increase, GE) using the aforementioned buffer. Fractions containing pure protein were pooled and concentrated to ~15 mg/mL, aliquoted, and stored at  $-80^\circ\text{C}$  until needed. For GST-TTL4, expression and purification were carried out in a similar manner, but Rosetta 2 cells were grown in TB medium with appropriate antibiotics.

### Purification of endogenous Nap1 from *Xenopus* egg extract

*Xenopus laevis* egg extract and low speed supernatant (LSS) were prepared as previously described.<sup>62</sup> Endogenous egg Nap1 (eNap1) was purified (see schematic, Figures S1A–S1E) from 10 mL of LSS supplemented with Neutravidin to a final concentration of 10 mg/mL. Histones H2A.S2 (bearing a C-terminal StrepII-tag, IBA Lifesciences) and H2B were expressed individually, purified under denaturing conditions, and refolded into dimers as described previously.<sup>63</sup> H2A.S2/H2B was added to Streptactin resin (IBA Lifesciences) pre-equilibrated in egg lysis buffer (ELB: 10mM HEPES-KOH pH 7.8, 50 mM KCl, 2.5 mM MgCl<sub>2</sub>) at ratio of 0.4 mg H2A.S2/H2B dimers per 1 mL Streptactin resin and incubated with rotation for 60 min at 4°C. The resin was then washed 3  $\times$  with 5 mL ELB and added to LSS at a ratio of 1 $\mu$ g H2A.S2/H2B dimers per 0.02 mL LSS and incubated with rotation for 90 min at 4°C. The resin was washed 2  $\times$  5 mL in ELB supplemented stepwise with 125 mM, 250 mM, 500 mM, 1 M, and 2 M NaCl. Both Nap1 and Npm2 were detected in the 0.5 M and 1 M NaCl fractions which were then combined. Npm2 was subsequently immunodepleted using Npm2 antibodies, as verified by immunoblot. eNap1 was buffer exchanged into 50 mM Tris-HCl pH 8.0, 25 mM NaCl, 5 mM  $\beta$ -ME and polished by size exclusion chromatography (Superdex 200 Increase, GE). Fractions containing pure eNap1 were pooled and concentrated to ~2 mg/mL (as measured by SYPRO Orange stain), aliquoted, and stored at  $-80^\circ\text{C}$  until needed. eNap1 was confirmed by immunoblot using anti-Nap1 and anti-Glu antibodies.

### Mass spectrometry

Digestion buffer was prepared with 100 mM ammonium bicarbonate, occasionally including 2 M urea buffer to mildly denature the protein, and the pH was adjusted to approximately 7.5 with 10% acetic acid. The samples of endogenous egg Nap1 or recombinant Nap1 were diluted 1:1 with digestion buffer. To reduce the disulfide bonds, dithiothreitol was added to the sample to a concentration of 2 mM and heated to 50°C for 30 min. Iodoacetamide was prepared and added to a concentration of 6 mM and incubated in the dark for 30 min. Endoproteinase Arg-C (cleaves c-terminal to arginine) or Trypsin (cleaves c-terminal to lysine/arginine) was added in a 1:100 (w/w) ratio with Nap1. Samples were incubated either at 25°C for 16 h or at 37°C for 6 h. Samples were frozen until they were evaluated by LC-MS/MS.

The samples were analyzed using in-house prepared columns. Both analytical and pre-columns were made of fused silica (360  $\mu\text{m}$  OD x 75  $\mu\text{m}$  ID for analytical and 100  $\mu\text{m}$  ID for pre-column) and had a 2 mm kasil frit. Analytical columns had a laser pulled tip. Two separate packing materials were used to evaluate samples: shorter peptides were evaluated with Dr. Maisch C18 packing material, both 3 and 5  $\mu\text{m}$  particle size, packed to 10 cm; larger peptides were evaluated with Agilent Poroshell, SB-C18 5  $\mu\text{m}$  particles packed to 10 cm. Reverse-phase separation was performed on an Agilent 1100 using 0.1% acetic acid for solvent A and 0.1% acetic acid in 60% acetonitrile for solvent B for short peptides or 0.2% formic acid for solvent A and 0.2% formic acid in 80% acetonitrile for solvent B for longer peptides. Gradients were run from 0-100% solvent B in 60 minutes at a flow rate of 100  $\mu\text{L}/\text{min}$ .

The preparatory columns were pressure loaded with 10 fmol equivalent of Pierce Retention Time Calibration Mixture and approximately 10-20 pmol of the digested material. The columns were rinsed with Solvent A prior to evaluation on a Thermo Orbitrap™ Fusion™ Mass Spectrometer. A full mass spectrum was acquired in the Orbitrap with 60,000 resolution at 200 m/z from 300 – 2000 m/z. Precursors were selected for fragmentation utilizing a decision tree process based on charge state and charge density (Figure S1F). Roughly, species with high charge density were fragmented by ETD; species with lower charge density were fragmented by CAD. Low-resolution MS/MS spectra were acquired for precursors with a charge state from +2 to +5, and high-resolution spectra were acquired for precursors with a charge state from +5 to +10. Precursors were excluded for 20 seconds after selection for fragmentation. Results were analyzed and manually validated using in-house developed software for fragment masses.

### Preparative chaperone glutamate-glutamylolation

Glutamylolation of Npm2 and Nap1 proteins was performed as previously described.<sup>9,30</sup> Briefly, 5 to 10mg Npm2 or Nap1 proteins (final concentration 2.5mg/mL) were mixed 1:100 with GST-TTLL4 (561-1199aa) in buffer containing 60mM Tris-HCl pH 8.5, 150mM NaCl, 10mM MgCl<sub>2</sub>, 2.5mM K+-L-Glutamate, 2.5mM ATP, and 5mM  $\beta$ -ME. Reactions were incubate at 30°C for 2 h then another 1:100 aliquot of GST-TTLL4 was added and incubation continued for another 2 h; one additional spike-in of GST-TTLL4 was added and the reaction was incubated for another 4 h. Glutamylolation was confirmed by immunoblot using the anti-Glu antibody.

### Competitive pull-down assays

For each sample, 10  $\mu\text{g}$  H2A.S2/H2B dimers were mixed with 25  $\mu\text{L}$  Streptactin Superflow resin in 200  $\mu\text{L}$  binding buffer (50 mM Tris-HCl, pH 8.0, 150 mM NaCl, 5 mM  $\beta$ -ME) and incubated with rotation at 4°C for 1 h. Resin only controls substituted binding buffer for H2A.S2/H2B. The resin was washed 3 x 500  $\mu\text{L}$  using the same buffer. 2.5  $\mu\text{M}$  chaperone proteins were added to the resin, either alone or mixed, in a final volume of 200  $\mu\text{L}$  and incubated with rotation at 4°C for 1 h. Each sample was washed with binding buffer 8 x 200  $\mu\text{L}$ ; resin was transferred to a new tube after the 8<sup>th</sup> wash and eluted with 25  $\mu\text{L}$  2x Laemmli Sample buffer. 10  $\mu\text{L}$  of eluate was separated by 15% SDS-PAGE and gels were stained with Coomassie Brilliant Blue. All experiments were repeated at least twice; a representative experiment is shown.

### Histone capture disaggregation assay

H2A/H2B dimers were mixed at a 20:1 molar ratio with a 500 bp linear fragment of DNA (final concentration 400 nM histones and 20 nM DNA) in a 20  $\mu\text{L}$  reaction volume in buffer containing 25mM sodium phosphate pH 7.0, 150mM NaCl, and 1mM EDTA. The reactions were incubated at 23°C for 15 min. Npm2 or Nap1 proteins were added, and the reactions were incubated at 23°C for an additional 30 min. 2.8  $\mu\text{L}$  of 50% glycerol was added to each reaction, and 10  $\mu\text{L}$  of each reaction was separated on 5% TBE native gel at 4°C for 45 min at constant 150 V. The gels were post-stained with EtBr. All experiments were repeated at least twice; a representative experiment is shown.

### Tetrasome and mononucleosome assembly assays

Tetrasomes were assembled by salt dilution by mixing 187 bp DNA, containing the 147 bp Lowary and Widom 601 sequence<sup>64</sup> flanked by 20 bp DNA on either end, with a 1.5-fold molar excess of (H3/H4)<sub>2</sub> in a buffer containing 50 mM Tris-HCl pH 8.0, 2 M NaCl, 1 mM EDTA, 10 mM  $\beta$ -ME, and 10% glycerol. The mixture was incubated at 37°C for 15 min then salt was diluted 10-fold (stepwise to 1.5, 1.0, 0.8, 0.7, 0.6, 0.5, 0.4, 0.3, and 0.2M NaCl) by the addition of salt-free buffer containing 50 mM Tris-HCl pH 8.0, 1 mM EDTA, 10 mM  $\beta$ -ME, 10% glycerol, 0.02% NP40, 1% PVA, and 1% PEG8K. The mixture was incubated at 37°C for 15 min between each dilution.

Mononucleosome assembly assays were carried out by combining Npm2 or Nap1 proteins with H2A/H2B dimers at a 2-fold molar excess of the tetrasome concentration in a 25  $\mu\text{L}$  reaction volume. Chaperone proteins and H2A/H2B were incubated at 30°C for 15 min in the absence of tetrasomes. Tetrasomes were added and the reaction was incubated at 30°C for an additional 15 min. 10  $\mu\text{L}$  of the reactions were separated on 5% TBE native gels at 4°C for 45 min at a constant 150 V, and gels were post-stained with EtBr. Nucleosomes assembled

by salt dilution with HeLa octamers<sup>30</sup> were included on the gel as a sizing control. All experiments were repeated at least twice; a representative experiment is shown.

### Fluorescence binding assays

Intrinsic tryptophan fluorescence of the unmodified or glutamylated Npm2 A2 peptides (DYSWAEDEE) in 20 mM Tris-HCl pH 7.6, 150 mM NaCl, 1 mM EDTA, 1 mM DTT, and 0.01% NP-40 was measured at 20°C in a Fluoromax-4 spectrofluorometer (HORIBA, Kyoto, Japan). The Npm2 peptide at 0.5 μM in a 0.1 × 0.1 cm quartz cuvette was excited at 295 nm using 5 × 5 nm slits. Emission spectra were collected in 1 nm steps between 305 nm and 450 nm using 0.5 s integration time per step. Background autofluorescence from buffer and histones was collected before addition of peptide and subtracted from spectra to obtain signal from the peptide alone. As previously described,<sup>9</sup> addition of histones resulted in a blue shift of the spectra, and data was plotted as the ratio of intensities at 340 nm and 360 nm (D340/360). Curves were converted to fractional saturation (Y) by normalizing D340/360<sub>min</sub> and D340/360<sub>max</sub> values to 0 and 1, respectively. Equilibrium dissociation constants (K<sub>D</sub>) and standard errors were then calculated by fitting the data to a single-site binding model taking the concentration of the peptide into account, as previously described:<sup>9</sup>

$$Y = \frac{(P+L+K_D) - \sqrt{(P+L+K_D)^2 - 4PL}}{2P}$$

Where Y is the normalized response (0-1), P is the Npm2 peptide concentration (0.5 μM), L is the concentration of histone H2A/H2B dimers, and K<sub>D</sub> is the equilibrium dissociation constant.

### Protein thermal shift assays

All thermal denaturation assays used H2A/H2B dimers at 0.5 mg/mL in 50 mM Bis-Tris propane pH 7.4, 150 mM NaCl, 1 mM EDTA, 1 mM DTT, and 10X SYPRO Orange. Denaturation assays were performed in a 384-well plate in a qPCR machine (Roche Lightcycler II) using a temperature range of 25-99°C, and fluorescence intensity was measured in 0.5°C steps equilibrating for 10 seconds at each temperature prior to reading fluorescence. Reactions were excited at 495 nm and fluorescence emission was recorded at 600 nm. Fluorescence curves were blanked with buffer without H2A/H2B dimers. Chaperone peptides and DNA were added in slight excess at a 1.2:1 molar ratio. Fluorescence of chaperone peptides and DNA were also measured in the absence of H2A/H2B, and showed no difference compared to buffer alone. Each reaction was split and measured five times. Fluorescence intensities with errors from three replicates were fit to the equation:

$$Y = \frac{(F_{max} - F_{min})}{(T_m - x)} \frac{1}{1 + e^{-n(x - T_m) + F_{min}}}$$

Where F<sub>min</sub> is the starting fluorescence and F<sub>max</sub> is the highest fluorescence intensity along the curve. T<sub>m</sub> is the melting temperature, and n is the cooperativity coefficient. The three replicates (each composed of 5 technical replicates) were used to calculate final T<sub>m</sub> values with standard error values, using the TSA-CRAFT algorithm.<sup>65</sup> One-way ANOVA tests were performed to determine significance of ΔT<sub>m</sub> values.

### Molecular dynamics simulations

All-atom, explicit solvent molecular dynamics (MD) trajectories were generated for the following four systems: (a) unmodified acidic IDR of Npm2 with H2A/H2B, (b) glutamylated acidic IDR of Npm2 with H2A/H2B, (c) unmodified acidic IDR of Nap1A3 with H2A/H2B, and (d) glutamylated acidic IDR of Nap1A3 with H2A/H2B. The Leap package implemented in AmberTools20 was utilized to parameterize the initial models of histone IDR/H2AH2B dimer.<sup>66</sup> The pdb4amber tool implemented in AmberTools20 was utilized to prepare the refined and optimized initial models to be used in subsequent Molecular Dynamics (MD) simulations. All MD simulations presented in this work were performed with Amber20 using Particle Mesh Ewald CUDA implementation (pmemd.cuda) and ff19SB force field.<sup>67</sup> All initial models were solvated in TIP4D water model with appropriate ions added to achieve neutrality. A solvent buffer of 15 Å was placed on all sides of each histone-peptide starting model. Periodic Boundary Conditions (PBCs) and Particle Mesh Ewald (PME) approximations for long-range interactions were implemented along with 9 Å cutoff for electrostatic interactions.

The implementation of minimization, equilibration, and production steps of all MD simulations consist of the following steps: (a) water and ions were minimized while other components were restrained with a positional restraint of 50.0 kcal/mol·Å<sup>2</sup>, (b) under constant volume, the system was slowly heated up from 100 K to 303.15 K over 10 ns of simulation time, (c) the system was kept at 303.15 K over 10 ns of simulation time at constant pressure, which allows the box density to relax, (d) keeping the system at 303.15 K at constant pressure, 5 ns of simulation was performed with a lower restraint of 10.0 kcal/mol·Å<sup>2</sup>, (e) minimization run was performed by applying restraint of 10.0 kcal/mol·Å<sup>2</sup> on only the backbone atoms, (f) the system was relaxed over 10 ns of simulation time under constant pressure conditions with backbone atoms restrained with a coefficient of 10.0 kcal/mol·Å<sup>2</sup>, (g) the system was relaxed over 20 ns of simulation time under constant pressure conditions by lowering the restraint on the backbone atoms to 1.0 kcal/mol·Å<sup>2</sup>, and (h) the system was further relaxed over 20 ns of simulation time under constant pressure conditions by lowering the restraint on the backbone atoms to 0.1 kcal/mol·Å<sup>2</sup>. Following this extensive minimization and relaxation protocol, production simulations with no restraints were run in the NPT ensemble at 1.0 bar and 303.15 K with an integration timestep of 2.0 fs for a simulation length of 1 μs. The Langevin dynamics collision frequency was set to 1 ps<sup>-1</sup> in production simulations. A unique random seed

determined by the system clock was used for each Langevin dynamics simulation. Simulated trajectory frames containing solute and solvent atoms were collected at 10 ps intervals for subsequent analysis. Frames from the simulated trajectories were processed using the CPPTRAJ<sup>68</sup> module in Amber20.

#### *Determining intermolecular contacts between histone IDR and H2A/H2B dimer*

Intermolecular atomic contacts between peptide IDR and histone H2A/H2B dimer were calculated from the simulated trajectory snapshots using INTERCAAT<sup>69</sup> using default settings.

#### *Clustering of structural ensembles of simulated trajectory*

To gain insight into the dominant conformations of IDPs a density-based conformational clustering approach was utilized,<sup>70</sup> with a cutoff value of 1.25 Å.

#### *Atomic fluctuation*

Atomic fluctuation of histone dimer H2A/H2B (in the presence and absence of peptide IDR) was calculated by first computing an ensemble average structure. This average structure was structurally aligned using CPPTRAJ module of the AMBER20 package to the first reference frame, and RMSD for each residue was measured.

#### **Labeling scheme and NMR analysis of the *Xenopus* H2A/H2B dimer**

H2A and H2B were expressed individually, purified under denaturing conditions, and refolded into dimers as described previously.<sup>63</sup> H2A and H2B were isotopically labeled using the Marley Method,<sup>71</sup> except that M9 minimal media was made with 100% D<sub>2</sub>O for the <sup>13</sup>C-<sup>15</sup>N-<sup>2</sup>H and <sup>15</sup>N-<sup>2</sup>H labeled samples.

All NMR experiments were performed at the New York Structural Biology Center and Albert Einstein College of Medicine on Bruker Avance III 600 MHz, 700 MHz or 800 MHz spectrometers running TopSpin and equipped with 5 mm cryogenically cooled triple resonance probes or on a Varian INOVA 600 MHz spectrometer running VnmrJ and equipped with a 5 mm cryogenically cooled triple resonance probe. All NMR data sets were processed on NMRbox<sup>51</sup> with NMRPipe<sup>49</sup> and analyzed using CcpNmr Analysis Version 2 software.<sup>50</sup> NMR samples were prepared in 25mM Na<sub>2</sub>PO<sub>4</sub> pH 7.0, 150mM NaCl, 1mM EDTA, 10% D<sub>2</sub>O, 0.05mM TSP and run at 25°C. For peptide experiments, the final DMSO concentration was no more than 0.5% by volume. Control experiments on labeled histones showed no HSQC chemical shifts with 0.5% DMSO.

For assignment 0.6mM of either <sup>2</sup>H-<sup>13</sup>C-<sup>15</sup>N H2A/H2B or H2A/<sup>2</sup>H-<sup>13</sup>C-<sup>15</sup>N H2B was used. Assignment of spectra from these two samples was accomplished by using a standard suite of triple resonance experiments (HNCO, HNcaCO, HNCA, HNcoCA, HNCACB, and HNcoCACB) utilizing TROSY-style pulse sequences and non-uniform sampling (NUS) methods<sup>49,72,73</sup> Resonances were assigned using a combination of PINE NMR server predictions and manual inspection of the spectra.<sup>74</sup>

All CSP experiments were performed in an identical buffer by collecting TROSY-HSQC spectra of 0.3mM <sup>2</sup>H-<sup>15</sup>N H2A/H2B or 0.3mM H2A/<sup>2</sup>H-<sup>15</sup>N H2B on a Bruker 600MHz spectrometer. Npm2 and Nap1 peptides were titrated by setting up multiple 50μL samples in 1.7 mm (about 0.07 in) NMR tubes and spectra were acquired using an autosampler. The Echo-Antiecho method with 2048 (t<sub>2</sub>) and 100 (t<sub>1</sub>) complex data points was used to acquire all the data, keeping the sweep width fixed at 14 and 32 ppm for <sup>1</sup>H and <sup>15</sup>N, respectively. A total of 64 scans and 32 dummy scans were recorded for each experiment.

Variable temperature experiments were performed by collecting TROSY-HSQC spectra using either 0.3mM <sup>2</sup>H-<sup>15</sup>N H2A/H2B or 0.3mM H2A/<sup>2</sup>H-<sup>15</sup>N H2B on a single sample. The Echo-Antiecho method with 2048 (t<sub>2</sub>) and 128 (t<sub>1</sub>) complex data points was used to acquire all the data, keeping the sweep width fixed at 14 and 32 ppm for <sup>1</sup>H and <sup>15</sup>N, respectively. A total of 16 scans and 32 dummy scans were recorded for each experiment. After temperature change, the samples were equilibrated for 20 minutes at the new temperature prior to collecting a TROSY-HSQC spectrum. Peak intensity changes and CSPs were calculated as described previously.<sup>9</sup>

#### **Histone peptide arrays**

Histone peptide array experiments were performed by JPT Peptide Technologies (Berlin, Germany) (Cat# His\_MA\_01). Binding events were probed by using a rabbit antibody raised against Nap1. Fluorescently labeled α rabbit IgG was used for detection of binding events. Signal intensities were scaled to the maximum intensity. Binding events on unmodified peptides were mapped onto a linear sequence of the histones.

#### **QUANTIFICATION AND STATISTICAL ANALYSIS**

All western blots, pull-down experiments, chromatin assembly assays, and binding assays were independently repeated at least twice. The thermal shift assays were performed in triplicate containing at least three technical replicates. Unpaired t-tests were performed for the thermal shift derived melting temperatures. All molecular dynamics simulations were performed twice, using independent starting positions. Gels were quantified in ImageJ.